Evaluation of the Effects of Molybdenum on Sulfur Deposition in Iron-Based Oxygen Carriers for Coal Direct Chemical Looping Processes

THESIS

Presented in Partial Fulfillment of the Requirements for Graduation with Honors Research Distinction in Chemical Engineering at The Ohio State University

by

Blaise R. Kimmel

B.S. Program in Chemical & Biomolecular Engineering

The Ohio State University

William G. Lowrie Department of Chemical & Biomolecular Engineering

2017

Thesis Committee:

Dr. Liang-Shih Fan, Advisor

Dr. Aravind Asthagiri

Abstract

Increasing demand of energy and global warming creates a challenging balancing case for fossil fuel based power generation plants. While mature carbon capture technology is already developed, the technology is often burdened with significant economic penalties. Coal direct chemical looping (CDCL) is an oxy-combustion process at The Ohio State University that successfully utilizes a counter-current moving bed and iron-based metal oxide oxygen carriers to capture carbon dioxide (CO_2) without incurring heavy costs. However, iron-based metal oxides in CDCL processes are susceptible to the formation of iron-sulfide (Fe-S) bonds, due to the presence of sulfur from coal. Sulfur deposition is known to decrease the reactivity of oxygen carriers and reduce metal carrier performance. In this study, molybdenum was investigated for its characteristics that preferentially enhance the adsorption of sulfur when compared with iron oxide. The goal of this study was to explore the kinetics of sulfur deposition with varying mixed metal-oxide concentrations. Thermogravimetric (TGA) experiments were studied at temperatures of 700ºC, 800ºC, and 900ºC with incremental iron-molybdenum ratios of binary powder mixtures. A 1:20 mixed volumetric ratio of hydrogen to 500-ppm hydrogen sulfide gases was utilized to reduce the binary mixture while encouraging sulfur deposition. X-Ray Powder Diffraction (XRD) was employed to qualitatively analyze the formation of both molybdenum-sulfide and iron-sulfide bonds. Experiments were conducted to assess the ability for molybdenum to selectively inhibit sulfur deposition on iron in the binary mixture. Although further testing is necessary to scale up the experiment, molybdenum has shown promise in slowing the formation of iron-sulfide bonds in CDCL processes. Enhancement of environmentally friendly combustion processes may allow for a lessened impact of fossil fuels, and ultimately a more efficient utilization of coal-derived energy.

Acknowledgements

I would like to thank my family, friends, and loved ones for their continual and untiring support and encouragement. Truly, this was not possible without you.

To my research advisor, Dr. Liang-Shih Fan, I would extend thanks for providing me with the opportunity to pursue undergraduate research. I credit the mentorship of both Dr. Fan and my graduate student, Cheng Chung, with helping me to become an independent, disciplined, and inquisitive scientist and guiding me toward a career in research.

To the other instructors and mentors that I have had during my time at Ohio State, I would offer thanks. You not only taught me the fundamentals of the discipline, but also through constant challenge, showed me how to become a successful engineer.

I thank the College of Engineering and the University Honors Program, as well. Their support, financial and otherwise, of my education is greatly appreciated.

I cannot forget about my many lab peers that have always assisted me in times of need or doubt or simply offered friendship. Some of those friends, in particular, include Brian Kulp, Mark Bartholomew, Serena Tabbaa, Lauren Pugh, Savannah Moses, and Lauren March.

Vita

2013.....Viera High School

2017.....B.S. Chemical & Biomolecular Engineering, The Ohio State University

Field of Study

Major Field: Chemical & Biomolecular Engineering

Table of Contents

List of Figures

List of Tables

Introduction

Climate Change and Air Pollution

Global warming is a leading environmental concern that is in part caused by carbon dioxide, CO_2, emissions from human activity. Fossil fuels, such as coal, oil, and natural gas, are currently the main contributors in the global energy market. These fuels are projected to make up 80% of the primary fuels utilized in the United States (US) by the year 2040 [1]. Trends of primary energy usage in the US over time are visualized in Figure 1. In 2015, the state of Ohio produced 5,306 GWh of electricity from coal that accounted for roughly 20% of the primary energy consumption across the US [2].

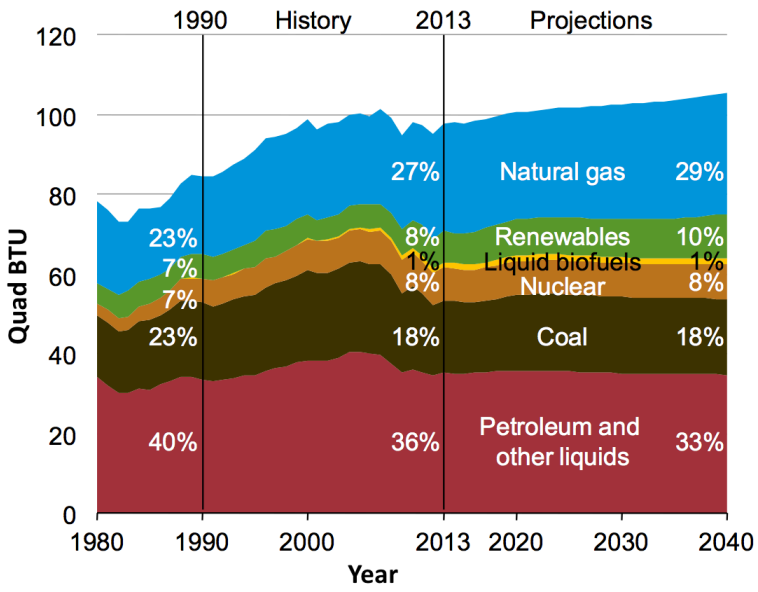

***Figure 1**: United States energy consumption in Quadrillion British Thermal Units (Quad BTU) vs. time [1].*

Fossil fuels are historically perceived to be in abundance. Furthermore, the simplicity in obtaining and harnessing the energy inherent to these fuels keeps the energy market dominated by fossil fuel powerhouses, such as ExxonMobil and Shell Petroleum. Fossil fuels remain a vital component of annual primary energy consumption due to both the sizable volumetric and gravimetric energy densities found in fossil fuels and the efficiency of technology used to convert the fuels to usable energy to power an ever-growing society of consumers. Although projected usage of renewable energy is shown in Figure 2 to increase by 25% from today to 2040, the challenges inherent to capturing renewable energy from sources such as the sun, water, and nuclear reactions are currently insurmountable with regional, technological, and ethical restrictions.

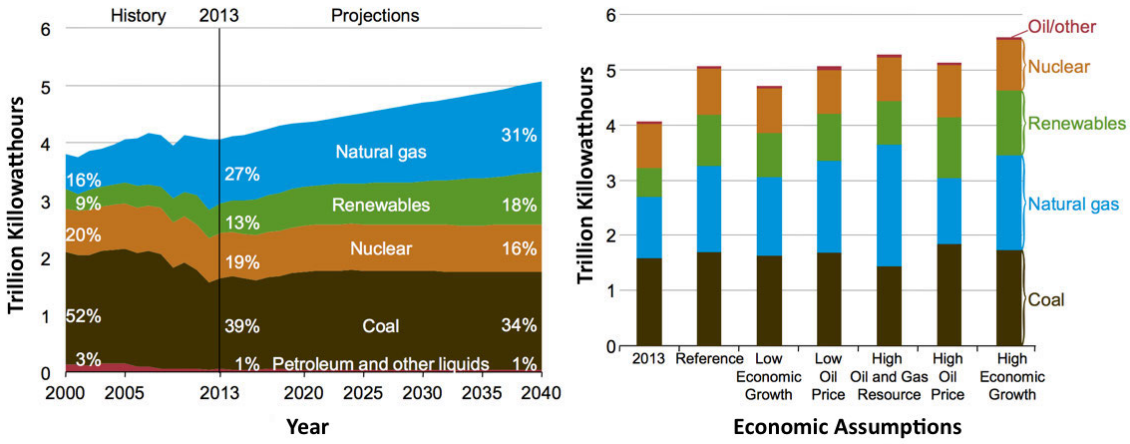

***Figure 2**: Electricity generation by fuel vs. time (left) and vs. various economic assumptions in the year 2040 (right) [1].*

Regional differences between the Midwest and coastal regions limit the areas from harnessing types of renewable energy, such as hydraulic energy. This limitation is due to a restriction in the availability of stored potential energy derived from an ocean, river, or waterfall. On the other hand, nuclear energy does

not have a regional limitation as power plants can be built in all environments. Harnessing nuclear energy brings about two main ethical concerns, the effect of nuclear waste on the environment and the dangers of runaway reactions near communities. In 1982, the Environmental Protection Agency (EPA) created the Summary of the Nuclear Waste Policy Act to designate repositories for the storage of radioactive waste caused from the usage of nuclear power [3]. To this day, amendments are still added to the act in order to decrease the opportunity for lasting effects of nuclear decay on animal and plant life near repositories, such as the addition of monitored retrievable storage facilities. Due to the chaotic nature of nuclear reactions, ethical debates are made to advance policies environmental safety and health policies to protect communities neighboring nuclear power plants [3].

Government policies directly affect the economic prosperity of energy consumption in the United States as well as the cost of imported oil. Regardless of economic assumption, coal-fired energy generation is projected to remain stagnant in the year 2040 with only one exception, a high usage of oil and natural gas as opposed to coal [1]. The importance of predicting future consequences of modern air pollution and controlling the release of harmful pollutants into the environment is imperative due to an overwhelming dominance in the projection of fossil fuels in future operations.

In the US, the use of fossil fuels such as those burned in coal-fired power plants contribute to the growing international crisis of climate change through an annual

emission level of 2.2 billion tons of CO_2 into the atmosphere [4]. The EPA acts as the controller of air pollution in the US by the implementation and regulation of policies. Additionally, the EPA provides maximum annual emission levels of toxins, such as CO_2, to the energy sector [2]. Figure 3 details the release of CO_2 per sector of energy consumption and provides a projection of emissions in the years 2025 and 2040 based on the reflection of emissions recorded in the years 2005 and 2013.

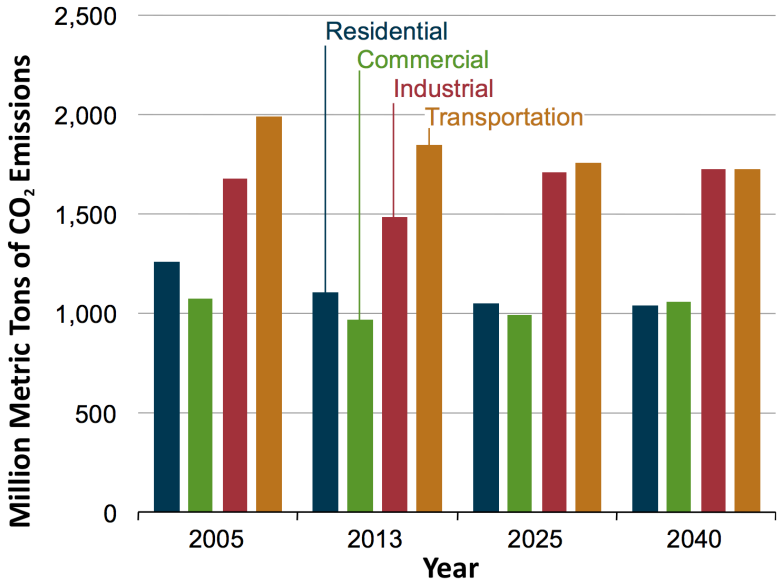

***Figure 3**: United States energy-related emissions of CO_2 in million metric tons per sector over time [1].*

In addition to the release of CO_2, other elements present in coal introduce a multitude of environmental challenges. Notable environmental challenges that emerge from coal-fired processes include the release of volatile mercury, the formation of particulate matter, and the consequential production and release of SO_2 [5].

Coal beds are formed in stages and vary on conditions of temperature and pressure. Assuming that temperature and pressure increase with increasing depth into the Earth's crust, there is a direct relationship to the age of the buried fossils. Figure 4 explores a graphical representation of various phases of coal and portrays the relationship between the conditions of fossils over time and the ranking of the formed coal. Notable trends include an increase in the density and heat value with an increase in the coal rank.

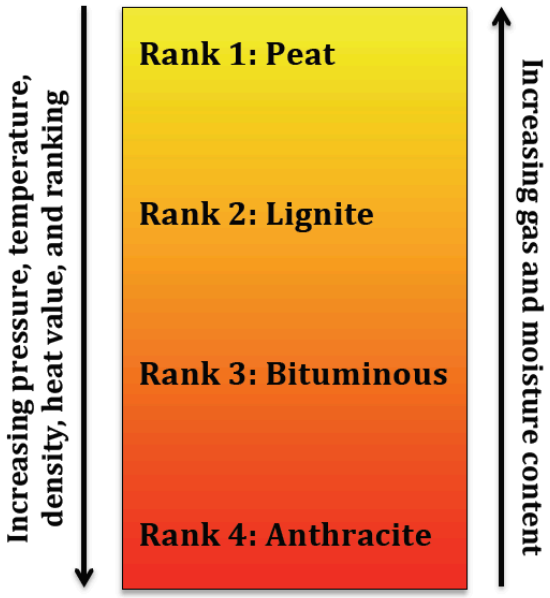

Figure 4*: Ranking of coal phases where the yellow area represents area closest to the surface of the Earth and the red area represents area deep under the crust.*

Most coal mined from Ohio lies in a bituminous phase and is deemed "soft coal" due to high conditions of pressure and temperature, plant life is ejected from the make up of the fossils [6]. The bituminous phase has the highest sulfur content of the four phases and when de-volatized the sulfur takes form of gaseous hydrogen sulfide, H_2S [7]. From coal-fired operations, H_2S is oxidized to sulfur dioxide

(SO_2), a critical pollutant, and is ultimately released to the environment. Once SO_2 is released into the atmosphere from stack emissions and transported by Gaussian plumes, various secondary pollutants, such as derivatives of sulfates, are able to form by atmospheric reaction and become harmful to the environment. An example of a secondary pollutant formed from SO_2 is sulfate based particulate matter (PM). When combusted in local Ohio power plants, bituminous coal produces levels above the national regulatory standard of $15\ \frac{\mu g}{m^3}$ for sulfate PM ambient concentrations [8].

Scrubbing processes are highly employed methods to decrease SO_2 emissions when added downstream of coal-fired power plant operations. However, the high cost of control equipment required to meet the standards and regulations set by the EPA limits the number of scrubbing units that should be installed to maximize company profits. Outside of environmental concerns, sulfur rich coal provides harmful design problems to plant operations, such as fouling of machinery in sulfur recovery units and the risk of sulfur fires and explosions [9].

Critical pollutants, such as SO_2 and PM, have the potential to become dangerous and adversely affect human health, welfare, and plant life at high concentrations. With the Clean Air Act of 1973, the US took control of the dangers present by the unrestricted annual release of copious tons of critical pollutants that rose from the industrial revolution [10]. The six critical pollutants identified by the EPA are portrayed in Figure 5.

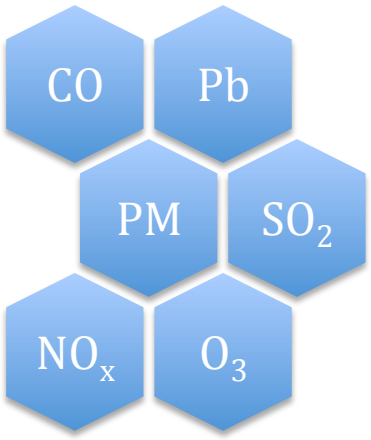

***Figure 5**: EPA critical air pollutants.*

National Ambient Air Quality Standards (NAAQS) were established by the EPA in the Clean Air Act for each of the critical pollutants and designates threshold concentrations of the pollutants in ambient conditions. These thresholds were made in tandem with the air quality index (AQI) to monitor the air quality in various locations across the country [11]. Figure 6 details the standard AQI figure used by the EPA to alert regions that are experiencing high concentrations of a pollutant so that sensitive groups may be informed and mitigations can be made to maintain a healthy lifestyle.

Air Quality Index Levels of Health Concern	Numerical Value	Meaning
Good	0 to 50	Air quality is considered satisfactory, and air pollution poses little or no risk.
Moderate	51 to 100	Air quality is acceptable; however, for some pollutants there may be a moderate health concern for a very small number of people who are unusually sensitive to air pollution.
Unhealthy for Sensitive Groups	101 to 150	Members of sensitive groups may experience health effects. The general public is not likely to be affected.
Unhealthy	151 to 200	Everyone may begin to experience health effects; members of sensitive groups may experience more serious health effects.
Very Unhealthy	201 to 300	Health alert: everyone may experience more serious health effects.
Hazardous	301 to 500	Health warnings of emergency conditions. The entire population is more likely to be affected.

***Figure 6**: Air Quality Index [11].*

The AQI provides a direct relationship between concentrations of air pollutants and health concerns for various groups of people, varying from healthy groups to sensitive groups. To measure the relationship and normalize the values for each of the six pollutants, a numerical value between 0 and 500 is assigned to the index where a value of 100 sets the "standard" threshold concentration for each pollutant.

Coal Direct Chemical Looping Combustion

The coal direct chemical looping (CDCL) process is a developing technology that economically captures CO_2 in fossil fuel-fired power plant through the combination of a circulating fluidized bed (CFB), moving bed reactor, and metal oxide engineering [12]. CDCL processes have been developed, focusing on the circulation of oxygen through the CFB with the use of metal oxides used as oxygen carriers, as to follow EPA regulations that focus on the oxy-combustion stage of power generation [13].

For CDCL, oxygen carriers circulate from a combustor to the reducer repeatedly in a loop, serving as a unit of time in defining the lifespan of carrier particles. When the carriers enter the reducer, fossil fuels such as coal-derived volatiles enter in either a co-current or counter-current direction to the metal carriers and ultimately reduce the metal oxide and release combustion products with high concentrations of both CO_2 and H_2O. The CO_2 air pollutant can be readily separated, captured, and sequestered in post-combustion unit operations [14]. When the reduced carriers move into the combustor, oxygen from the air stream

oxidizes and regenerates the carriers before returning to the reducer. Since oxidation is a highly exothermic reaction, electricity generation from the spent air is possible with conventional heat exchangers and steam turbines.

Visualization of the CDCL process is provided in Figure 7.

The reactions occurring in the combustor and the reducer used to first oxidize and then reduce the metal carriers, respectively, are also provided in Figure 7. In the figure, the green arrows represent the movement of air, the blue arrows represent the movement of the metal oxygen carrier, and the black arrows represent the counter-current flow of volatiles in the reducer.

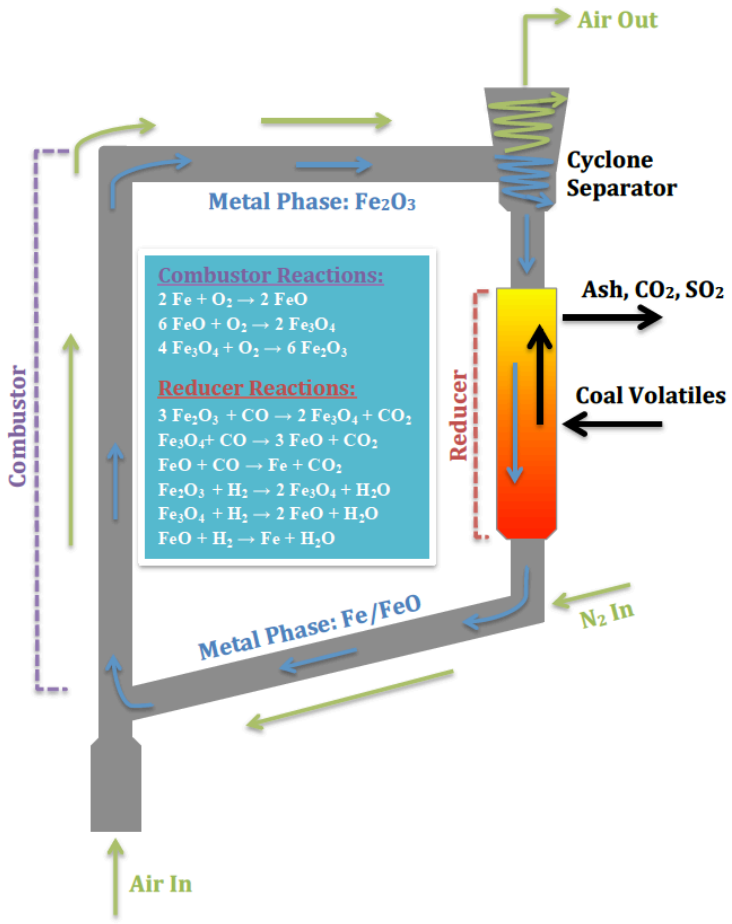

***Figure 7**: CDCL process utilized in the Fan laboratory.*

There are multiple benefits to this technology. These benefits include massive decreases in capital costs of equipment by creating the oxygen in-situ on the carrier, flexibility to upgrade the performance of the system to meet EPA regulations and requirements, and no loss in energy production from the plant [4].

For CDCL technology that utilizes iron oxide based oxygen carriers, formation of iron-sulfide (Fe-S) bonds can occur through chemisorption when the oxygen carriers come in contact with a sulfur derived species, and potentially reduce the reactivity of oxygen carriers with high-sulfur coal and affect the performance of the CDCL process [15] [16]. In order to employ CDCL technology in a variety of power plants, understanding the interaction between sulfur and iron-based oxygen carrier is crucial [4].

Reactor Design

Gas-solid fluidization is employed industrially to transform a normally fixed bed of particles with a passing fluid stream into a bed of particles with fluid-like properties, ultimately allowing for increased heat and mass transfer in a controlled, low pressure, flow regime [17]. Fluidization of particle beds has been applied to industries, including coal power plants, through modification of the fluidization process by the introduction of catalytic reactor units. This CDCL process follows the design characteristics of a circulating fluidized bed (CFB) [4].

In a fluidized bed, solid particles become suspended as a result of a gas or liquid flowing upwards through the particles [18]. As the superficial fluid velocity of the

fluid increases, the solid particles experience an increasing drag force that counteracts the force of gravity as the flow pushes against the bottom. The free body diagram in Figure 8 illustrates the forces acting on each particle in a packed and fluidized bed.

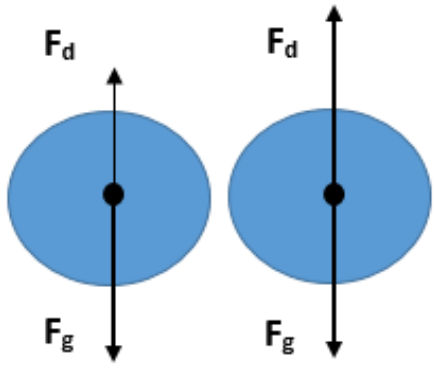

***Figure 8**: Force balance for particles. The particle on the right will act like a fluid because the drag force, F_d, will counteract the force of gravity, F_g. When F_d is not as large as F_g (left), the particles will act as a packed solid.*

Fritz Winkler first realized the practicality of fluidized beds in 1922 through the creation of a fluidized bed gas generator for coal gasification [19]. Although the technology spent two decades with relatively little use, the widespread application of this technology was catalyzed when Standard Oil of New Jersey, now known as ExxonMobil, implemented a fluidized bed reactor in a catalytic cracking unit in 1942 at a Baton Rouge Refinery [20].

Catalytic hydrocarbon cracking has since become the most important use of fluidized beds, as it permits the transformation of heavy crude oil into more valuable short-chain hydrocarbons at a scale of over 10 million barrels of crude

oil per year worldwide [21]. Figure 9 presents a number of other uses for fluidized beds.

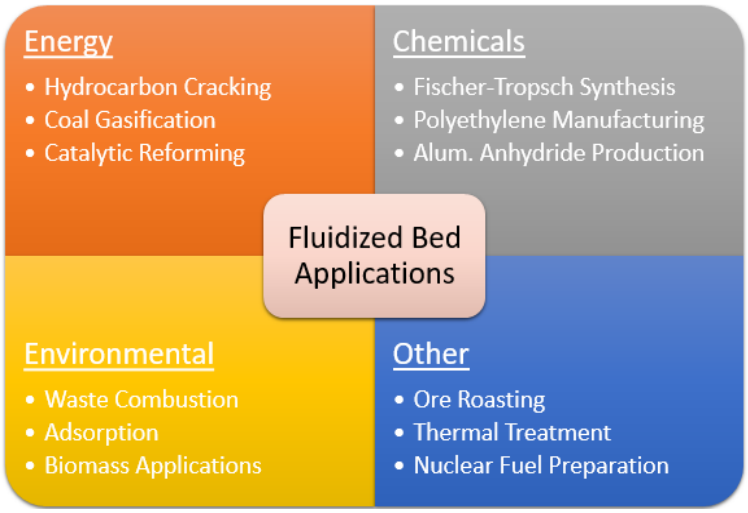

***Figure 9**: Subset of the dozens of industrial applications of fluidized beds [22].*

Fluidized bed reactors (FBRs) compete with a number of other reactor types for use, and as with almost any technology, both advantages and disadvantages exist. Figure 10 presents the main advantages and disadvantages of FBRs.

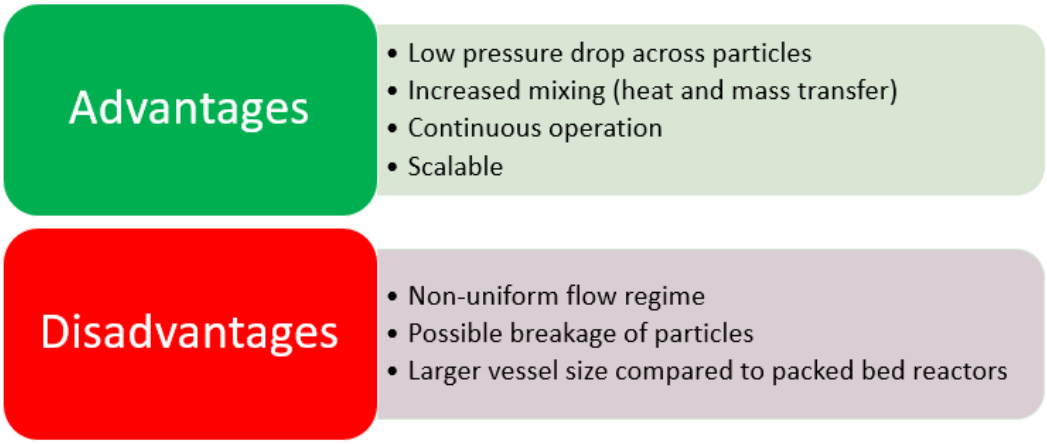

***Figure 10**: Pros and cons of FBRs. Note that while the increased mixing causes greater heat and mass transfer, it also can lead to non-ideal mixing and thus lower conversion rates for catalytic reactions [23].*

As shown in Figure 10, one of the most important advantages FBRs exhibit over other reactors is increased heat and mass transfer, which is often critical to the successful conversion of a reactant with catalyst particles. The extent of this transfer stems from the type of fluidization occurring within the FBR. Two general types of fluidization: particulate and bubbling, are typically observed [24].

Particulate fluidization occurs when the bed expands as a result of increasing fluid velocity. This type allows the solid particles to remain approximately homogenous and promotes intimate contact between the fluid and the particles as a result of the increased surface area of the solid. Consequently, the fluidized beds exhibits higher heat and mass transfer coefficients [23]. For this reason, particulate fluidization is desirable in many industrial applications. On the other hand, bubbling fluidization leads to the formation of pockets of air within the bed, which reduces the amount of contact between the fluid and the particles. Bubbling fluidization can even lead to slugging, in which the bubbles coalesce to sizes approaching the diameter of the reactor and can lead to large pressure fluctuations and loss of catalyst [23].

The CDCL process, developed at The Ohio State University, is industrially novel by the integration of a CFB and a moving bed reactor. The reducer utilizes a moving bed reactor to improve the purity of CO_2 produced from CO the process at high temperatures, as visualized the plot in the center of Figure 11. While moving bed reactors are not well mixed, the high purity production of CO_2 leads to efficient capture and sequestration of CO_2 with post-combustion scrubbers [4].

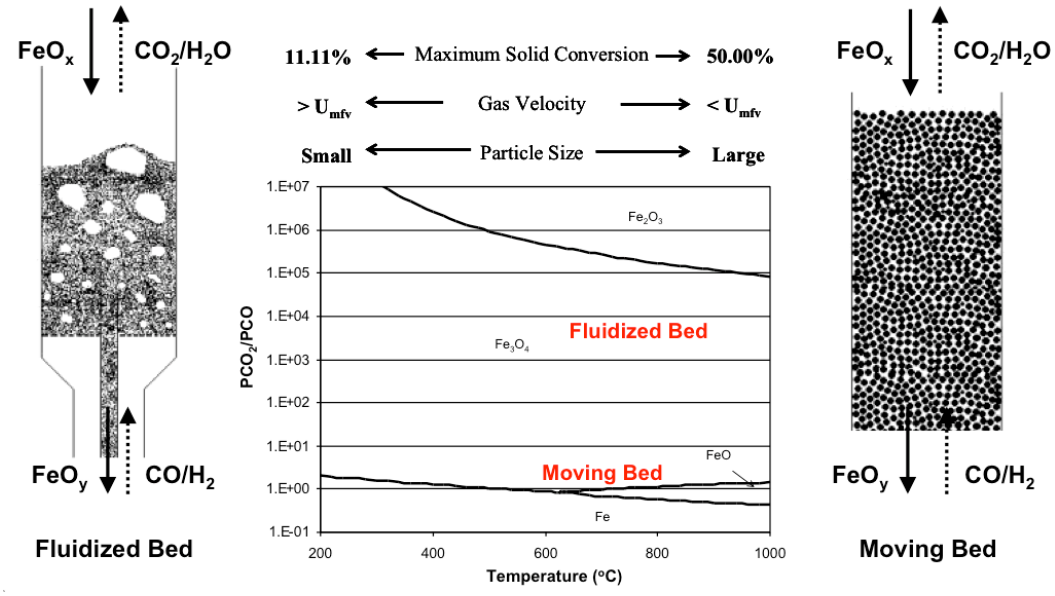

***Figure 11**: Comparison of fluidized beds to moving beds [4].*

Literature Review

The primary concern entering the project is the identification of a metal additive that selectively inhibits sulfur poisoning of metal oxygen carriers. The three main mechanisms of sulfur poisoning involve sulfur adsorption and consequential reaction site blockage, electronic modification to neighboring metal atoms, and the restructuring of the metal surface such that reactions between iron and hydrocarbons are hindered [16].

Specifications of the metal additive include the need to slow the formation of Fe-S bond formation through adsorption and ultimately elongate the lifespan of the metal oxygen carrier. There are two crucial elements considered in the selection of a viable additive. First, added metals must maintain the characteristics of a strong sulfur acceptor by selectively adsorbing sulfur when in the presence of the

carrier metal. Second, if the additive does not exhibit properties of selectively adsorbing sulfur atoms, it is desirable for the metal additive to decrease the rate of formation of Fe-S bonds with respect to a decrease in the concentration of iron in the metal oxygen carrier [16]. Initial thermodynamic studies collected from the Fan group indicate that the presence of steam in the reducer acts to initially inhibit the formation of Fe-S bonds on metal oxygen carriers and that the H_2S gas equilibrium concentration is inversely proportional to the oxidation state of iron [25].

Metal additives, such as molybdenum, have shown potential in literature to slow the formation of Fe-S bonds and thus act as an inhibitor by selectively adsorbing sulfur, such that the iron metal may continue transporting oxygen from the combustor to the reducer [16]. Molybdenum is known to selectively adsorb sulfur species from sour natural gas through a mechanism referred to as hydrodesulfurization (HDS) [26].

HDS is utilized in catalytic processes to selectively poison the molybdenum metal as to prolong the lifespan of other chemical components. Simultaneously, this process shows potential to reduce SO_2 emissions by releasing the adsorbed sulfur to an external source when regenerating the particle with respect to safety and health hazards inherent to the formation of SO_2 [27].

Through literature, introducing a metal additive into the makeup of oxygen carriers is shown to increase the sulfur tolerance of the particles within the

process. Metal additives present the opportunity to extend the lifespan of the iron oxide particles in the reactor bed and decrease the release of critical pollutants, such as SO_2, into the atmosphere as a by-product of coal-fired energy generation.

Experimental Methodology

General Overview

In order to simulate sulfur poisoning of iron and molybdenum binary mixtures, experimental methods were developed. Phase I of this study involved the synthesis and testing of the control particle, A, under several different temperatures in the thermogravimetric analyzer (TGA). In Phase II, binary metal mixtures were formed with batches following mass weight ratios of 4:1, 2:1, and 1:1 of iron-III to molybdenum-VI.

To study the reduction of the particles that occurs in the reducer, pre-oxidized metals were synthesized. Carrier particles were tested under conditions similar to the reducer in the CDLC process by flowing a mixture of hydrogen sulfide gas, H_2S, and nitrogen gas, N_2, into the TGA and reacting isothermally at 700, 800, and 900ºC. A diagram of the metal compositions formed with the three reactor temperatures employed in the TGA can be found in Table 1.

Table 1: *Plot of the 12 trials performed.*

	700ºC	**800ºC**	**900ºC**
Control Group, Only Fe-III	Control Group at 700ºC	Control Group at 800ºC	Control Group at 900ºC
4:1 Fe-III to Mo-VI	4:1 Ratio at 700ºC	4:1 Ratio at 800ºC	4:1 Ratio at 900ºC
2:1 Fe-III to Mo-VI	2:1 Ratio at 700ºC	2:1 Ratio at 800ºC	2:1 Ratio at 900ºC
1:1 Fe-III to Mo-VI	1:1 Ratio at 700ºC	1:1 Ratio at 800ºC	1:1 Ratio at 900ºC

In Table 1, metal compositions formed in the ball mill are organized on the y-axis and the TGA reactor conditions lie on the x-axis at ambient pressure.

In order to analyze the compositions of the particles before and after reaction in the TGA, powder x-ray diffractometer (XRD) was employed. Data collected from the instruments and testing methods were integrated, analyzed, and simulated to select the optimal additive concentration, on a binary mixture basis, to increasing sulfur tolerance of Fe_2O_3.

List of Materials and Equipment

This research experiment included materials listed in the following set:

1. Iron-III Oxide: Fe_2O_3
2. Molybdenum-VI Oxide: MoO_3
3. Dilute acetic acid
4. Tap water
5. Distilled (research-grade) water
6. Dish soap

Equipment used in this research experiment can be found listed in sets that are organized by experimental area:

1. Ball Mill Area
    1. Ceramic mill jar
        a. Gaskets
        b. 30 ceramic round pellets
    2. Mechanical rolling mill and actuator apparatus
    3. Weigh-boats
    4. Ceramic boat
    5. Glass vials
    6. Mass balance
    7. Scrub brush and scraping instruments
    8. Glass pan
    9. Sintering oven
2. TGA Area
    1. Pyris Thermogravimetric Analyzer (TGA)
    2. Metal mass balls
    3. Crucibles
    4. Mass flow controllers and manifold
    5. Computer with pre-programmed software to collect data
3. Center of Electron Microscopy and Spectroscopy (CEMAS)
    1. Sample wafer and holder
    2. Computers with pre-programmed software to collect data
    3. Rigaku Smart Lab: XRD

Ball Mill Experiment

After purchasing a 100g sample of 99.9% molybdenum trioxide (MoO_3), the two distinct phases of metal-oxygen carriers were synthesized: I. (Fe_2O_3) and II. (Fe_2O_3)/(MoO_3). In order to specify the particles formed in Phase II, a label of 'ax' was added to the end of the batch name where 'x' is representative of a lowercase roman numeral. An example of a name for a batch in Phase II is 'Phase IIa.i.' The specific weights of particles synthesized, on a 30g basis, can be visualized in Table 2.

Table 2: *Concentrations of particles synthesized on a 30g basis. Particles are assumed to be in an oxidized state previous to mixing.*

	Phase I	**Phase IIa.i**	**Phase IIa.ii**	**Phase IIa.iii**
Fe_2O_3	30g	24g	20g	15g
MoO_3	0g	6g	10g	15g

Phase I acted as the control group while the concentration ratio of iron to molybdenum was varied in Phase II, acting as the experimental group. Particles formed in Phase II were assumed as binary metal mixtures at a size range of 5-10 μm [29]. The current method of forming the carriers on a bench scale involves milling and mixing binary metal mixtures with a laboratory scale ball mill for 24 hours [30]. In order to allow for proper mixing of the two metal elements, the particles crafted in this experiment were milled for 24 hours. The ball mill experiment used two primary pieces of equipment: a size 'o' ceramic mill jar with 30 ceramic balls, each at a diameter of 1.5 cm, and a mechanical ball mill grinder. A close-up image of a ball mill can be found in Figure 12.

Figure 12: *Depiction of mechanical rolling mill and actuator apparatus.*

In the grinding process, the prepared chemicals were combined in a ceramic mill jar with ceramic balls in order for the materials to be ground to a colloidal fineness of roughly 5-10 µm. By increasing the surface area of these materials, the rate of mass transfer, and consequently the rate of reaction, at the interface between the reducing agents and the metal oxides within the TGA are assumed to increase. In the mechanical grinder, the ceramic balls cascade due to the centrifugal force applied to the outer walls of the jar from the slow rotation of the supporting wheels at the base of the jar. This force of the balls allows for the materials within the mill to be mixed evenly and dispersed into fine particles. A depiction of the grinding process can be found in Figure 13.

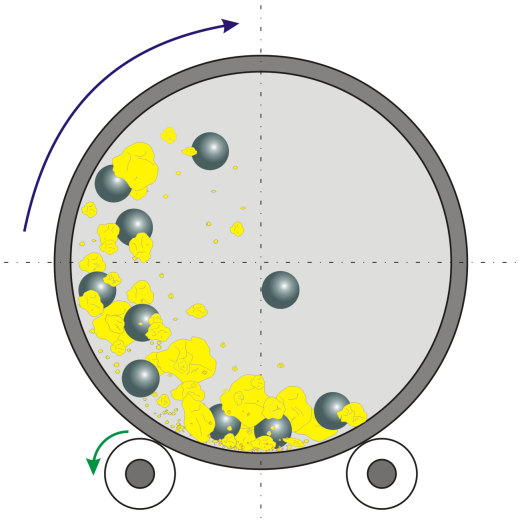

Figure 13: *Depiction of the grinding process within a mill jar [31].*

In order to study the various properties inherent to the interaction of molybdenum and sulfur, the particles formed in the ball mill were sintered at 900ºC for 12 hours. After being treated by heat in the sintering stage, a well-distributed lattice structure of the two metals was formed [32]. This lattice structure allowed for the assumption of a binary metal mixture of iron and molybdenum. The differences in the non-sintered and sintered particles and the reasoning behind the significance of sintering before experimentation will be explored further in the *Results and Discussion* section.

Ball Mill Procedure

Sequence of Operations

1. For each trial, the required respective weights of MoO_3 and Fe_2O_3 were measured in separate weigh-boats. Before loading samples onto the weigh-boats, the boats were placed on the balance and zeroed to provide a

differential basis between the weigh-boat and the material. Once zeroed, the samples were loaded and massed by an analytical balance, as illustrated in Figure 14.

Figure 14: *Photograph of the analytical balance utilized in the Fan laboratory.*

2. Once the materials were weighed for each trial, the samples were combined in a ceramic mill jar with 30 ceramic round pellets. The mixture of oxidized metals and pellets were manually shaken for one-minute by the researcher prior to the grinding process to ensure proper pre-mixing of the materials. A picture of the ceramic mill jar can be found in Figure 15.

Figure 15: *Photograph of the ceramic mill jar.*

3. The ceramic mill jar was then placed on the rolling ball mill and the actuator was switched to the ‘on’ position to begin the rolling operation. A 24-hour rolling period was given for each trial to allow for proper mixing of the materials.
4. At the completion of the rolling process, the sample was extracted from the ceramic mill jar by scraping the sides of the jar. The mixture was then collected in a large ceramic crucible.
5. Once collected in the crucible, the samples were sintered in the sintering oven for a 12-hour period at 900ºC to treat the particles with heat prior to reactor operations.
6. After sintering, the particles were collected in a vile and labeled for future experimentation in the TGA.

TGA Experiment

In order to properly model the reaction that occurs in the reducer, an isothermal reactor reduced the oxidized particles. By studying the reduction of particles at various isothermal reaction temperatures, the kinetics of the reduction reaction can be examined. A detailed investigation of the reaction kinetics is located in the *Results and Discussion* section.

From preliminary experimentation, time-scales were chosen to allow enough time for each phase of iron to emerge as Fe_2O_3 reduced to Fe and to allow deposition of sulfur to be distinctly observed. With decreasing reactor temperatures, an increase in the amount of time allotted for isothermal reaction was needed. Table 3 provides the time required for isothermal reaction for each of the chosen reactor temperatures. Notice that an interval time difference of eight additional minutes was necessary for every 100ºC decrease in reactor operation temperature. The reaction kinetics of the experiments influenced time interval differences that will be further explored in the *Results and Discussion* section.

Table 3: *Time scale for TGA operations based on the operation temperature.*

700ºC	800ºC	900ºC
125 minutes	117 minutes	109 minutes

Preliminary experiments aided the researcher in determining the proper ratio of reducing gases. By over-weighting the ratio of hydrogen gas (H_2), the reaction occurred too quickly to adequately make a qualitative analysis of the mechanism. Alternatively, by charging the reactor with a high ratio of hydrogen sulfide, the

kinetics of the reaction were too slow to observe sulfur deposition on a reasonable time scale for this study. After several experiments, the ratio of H_2 to H_2S was determined to be 1:20, allowing the researcher the opportunity to realize the reduction at all phases of iron and observe a noticeable deposit of sulfur to the surface of the particles. The TGA used for this study can be found in Figure 16.

Figure 16: *Pyris TGA.*

TGA Procedure

Sequence of Operations

1. The computer program used to control the mass flow controllers (MFC) on the manifold was started up. Specifications of each compound and respective volumetric flow rates were set for each MFC. A picture of the manifold used for this experiment is shown in Figure 17.

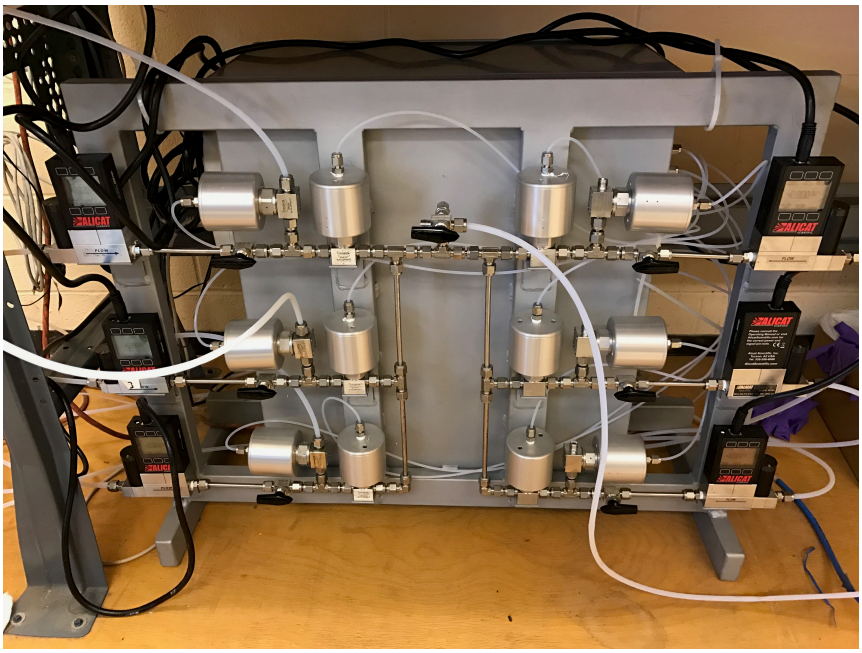

Figure 17: *MFC manifold.*

2. The pressurized tanks and regulators for each of the compounds necessary for experimentation were opened. Following the tubing from the tanks to the manifold, all valves were manually set to the 'open' position.
3. Nitrogen gas (N_2) was set to 50 mL/min at all points in the experiment to purge the reactor after the reduction stage took place and to help stabilize the TGA.
4. The computer software used by the TGA to track differential mass changes was started up and the experiment was initialized. In the software, the times required to heat the reactor to the maximum operating temperature, react at the isothermal condition, and cool down were all then set by the researcher. A visual representation of this program can be found in Figure 18.

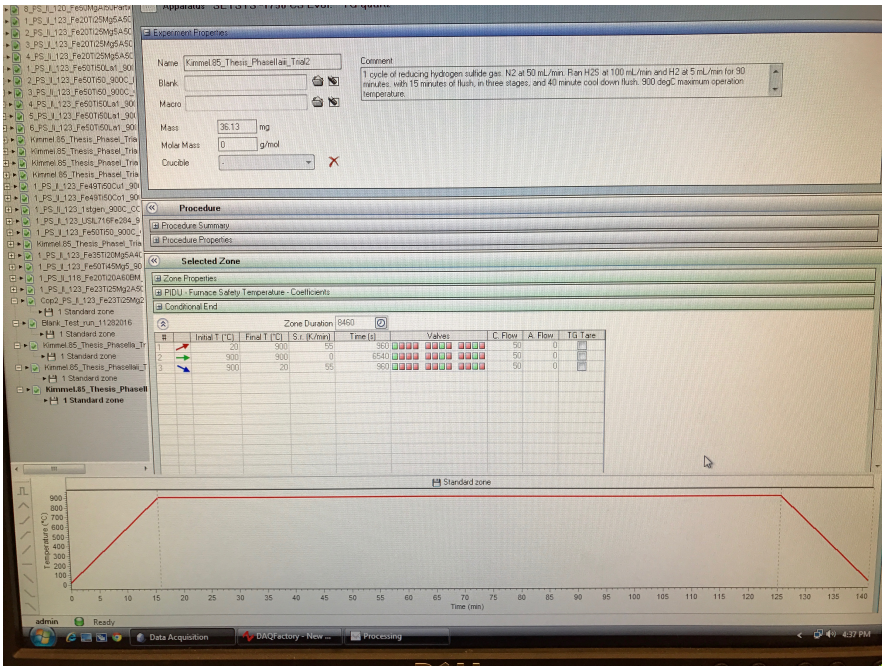

Figure 18: *TGA program used to initialize the experiment.*

5. The TGA was then loaded with an empty crucible. After a 10-minute period, the TGA stabilized. At this point, the researcher set a ‘tare’ for the TGA to ‘zero’ the weight of the crucible so that a differential weight could be taken of the particles that would be loaded onto the crucible.
6. Particle samples were loaded onto the crucible and the system was allowed to stabilize for another 10-minute period. The weight of the sample was recorded.
7. Once the researcher checked to ensure that all proper safety procedures had been followed and the experiment was properly set up, the experiment started.
8. At the completion of the experiment, the crucible with the reacted sample was taken from the TGA. Special care was taken to ensure that the sample

was not retrieved from the TGA until the system temperature dropped below 30ºC.

9. The sample was collected in a vial and labeled for future experiments.
10. The valves on the tubing for each of the chemicals used were set to the 'closed' position. The tanks and regulators were then closed.
11. Images of the differential mass of the sample during reaction were saved into a folder for the researcher. Once the images were obtained, the computer program was closed.

CEMAS Experiment

The instrument utilized in the CEMAS was the XRD. X-ray powder diffraction is a technique used to analytically identify phases present in a crystalline material. By generating x-rays in a cathode ray tube, electrons are able to be projected at homogenized particles and excite inner shell electrons [33]. A visual representation of the electron rays exciting particles in the XRD can be found in Figure 19.

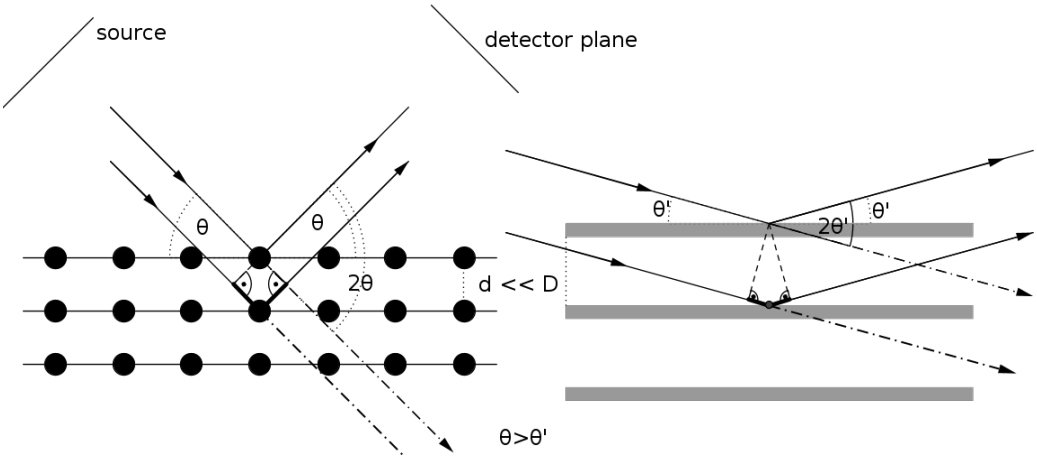

Figure 19: *Angles formed by incident and diffracting electron rays [34].*

Using wave physics, the angles at which the electron rays are incident to the particles are recorded. The angles produced by the electron rays that diffract from the particle, after the electrons in the lattice structure are excited, are observed in this instrument. The comparison of these two angles allows for a continuous computation of the wavelength for the electrons ejected from the particles. After processing the many wavelengths collected at various incident angles, a plot is made. The particle composition can be characterized by comparing distinct peaks in the plot to those found in literature for the locations of specific phases.

CEMAS Procedure

Sequence of Operations

The researcher studied the effects of sulfur deposition on the surface of the metal oxygen carriers by utilizing the XRD. The procedures followed for both of these instruments are provided in the next two sub-sections.

XRD Procedure

1. The computer program used by the instrument to analyze the samples was started up. The instrument was automatically calibrated during the start up process.
2. Sample particles were loaded onto a wafer and placed in the XRD instrument.
3. By executing a trial, the sample was continuously analyzed by the instrument and a respective plot of wavelengths against various incident electron ray angles was made.

4. Using the software, peaks were analyzed to identify the characteristic phases of the sample.
5. Once all trials were completed, the wafers were cleaned and the instrument was shut down.

Data Analysis

Once the experiment was completed, the researcher analyzed the data to attempt to discover a variety of trends and operating parameters. These values, as well as a discussion on the mechanisms at work to produce them, can be found in the *Results and Discussion* section.

Variable Testing and Rationale

The independent variables tested in this experiment were the concentration weight ratios of the two metals and the operating temperature of the TGA. Dependent variable data were collected from two sources: the TGA and the XRD. For the TGA experiment, data collected were in a graphical form depicting changes in the mass of the particles over time. By studying the change in mass for the particles, the researcher could determine how much oxygen was desorbed by the reducing agent, track the oxidation state of the metal, and ultimately visualize sulfur deposition on the surface of the particles.

The flow rate of the reducing agent and the reactor temperature were both held constant throughout the reduction stage of the experiment. X-ray powder

diffraction was performed in the XRD on the reacted particles to study the resulting reduced phases of particles from the TGA and to observe the effects of the independent variables on the formation of Fe-S and Mo-S bonds.

Analysis Methods

After testing the variables mentioned in the previous section, an analysis was performed on the data obtained. Due to the scope of this research, the only calculations that could be performed were theoretical in the kinetics section of this study. Qualitative analysis of the results obtained from the TGA and XRD were the focus of this research. After completing the analysis, conclusions were drawn from the experiment as a whole, and future recommendations were proposed.

Safety and Hazard Analysis

Personal Protection Equipment (PPE)

A preventative safeguard applied in the laboratory required the appropriate usage of PPE. Safety data sheets (SDS) stated to use the following PPE:

- Hard Hat
- Safety Glasses/Splash Goggles
- Closed Toe Shoes
- Long Sleeved Shirt/Lab Coat
- Long Pants
- Thermal Gloves
- Nitrile Rubber Gloves (when handling acidic solutions)

PPE was worn at all times within the Fan laboratory and CEMAS to protect the safety of the researcher. Loose fitting clothing and other loose accessories were restrained. In addition, no jewelry or contact lenses were worn in accordance with the SDS.

Equipment Safety

Researchers were aware of the various risks and hazards inherent to the operation of the equipment necessary to perform the experiments required for this study. In order to promote a culture of safety, various safety considerations were followed and all equipment was handled with care. These considerations are described in the following sub-sections with respect to each of the three main experimental areas, in addition to general areas in the laboratory.

Ball Mill Room

- High rotation speeds are a danger with the use of the ball mill. Proper care was taken by the researcher in positioning the ceramic mill jar to decrease the opportunity for the jar to be launched off of the rolling belt and make impact with other equipment in the room or a researcher.
- Acetic acid had the opportunity to be a flammability hazard if the lower flammability limit had been reached and a proper ignition temperature was made available. While the flash points of the chemicals were not reached within experimentation, researchers were aware of the flammability hazard from the SDS.

- Operation of the sintering oven required the use of thermal gloves to avoid burning exposed skin. Researchers made use of proper PPE when performing sintering experiments.

TGA Room

- While the hydrogen sulfide gas was highly dilute, special care was given to experimentation when utilizing the chemical. Proper ventilation was provided in the design of the reactor area. If one was to come into contact with either of the chemicals, the team was prepared to safely move away from the area of operation and evacuate all personnel. In order to continuously monitor the exposure level of hydrogen sulfide, a sulfur sensor was used with the function being to alert the researchers if the concentration of hydrogen sulfide exceeded 10 ppm.
- High-pressure buildup in the tubing could have occurred if the regulators failed. Leaking of the reacting chemicals would be a consequence of this due to a rupture in the tubing of the line.

CEMAS

- Equipment was properly used when performing XRD experiments, taking care to avoid the destruction of any materials.
- In order to decrease the opportunity for accidental ingestion of chemicals, food was not permitted in the CEMAS facility when operating the XRD.
- Radiation is an inherent hazard associated with the use of the XRD. In order to limit exposure to x-ray radiation, the researcher took appropriate precautions to decrease contact time with radioactive materials.

General Areas

- While ventilation was in place within the Fan laboratory, researchers were aware of the fumes that may emit from the use of hydrogen sulfide. Headache and nausea were possible symptoms of overexposure to the gas. Researchers not involved in the study were made aware of the hazard and informed of proper evacuation procedures in the event of a hydrogen sulfide tank leak.
- Running was not permitted in the Fan laboratory as a researcher may have encountered one of the following problems:
    - Slip, trip, and falls
    - Becoming injured from abrasions or deeper impact injuries
    - Being struck by passive or active machinery

Evacuation Safety

In the event of an emergency, the researcher was to refer to the evacuation safety guidelines obtained from the laboratory. Under the direction of the superior researcher, the research team was prepared to carry out emergency shutdown procedures for the experiment, follow evacuation routes, and safely wait for further instruction at the emergency assembly point. If an emergency did occur, the following actions would have occurred:

1. Follow the emergency shutdown procedure found within the laboratory.
2. Inform the safety champion of the emergency.
3. Evacuate the laboratory, following the directions of the safety champion.

Safety Data Sheets (SDS)

In order to promote a culture of safety for researchers, it is important to be aware of the risks and hazards inherent to the materials and chemicals used in the laboratory. Links to the SDS for compounds encountered in this study are listed in Table 4.

Table 4: *Links to SDS.*

Compound	Link to SDS online
Fe_2O_3	http://www.sigmaaldrich.com/catalog/product/sigald/203513?lang=en&region=US
MoO_3	http://www.sigmaaldrich.com/catalog/product/sigald/267856?lang=en&region=US
Tap Water	http://www.needlers.co.uk/media/mconnect_uploadfiles/z/0/z0209_safety_data_sheet.pdf
Dawn Dishwashing Soap	http://pgpro.com/brands/dawn/dawn-dishwashing-liquid/
Acetic Acid	http://www.sciencelab.com/msds.php?msdsId=9922769
Distilled Water	http://www.azerscientific.com/lanotattachments/download/file/id/133/store/1/sds-deionized_water-es616.pdf

Results and Discussion

General Observations

Prior to experimentation in the TGA, particles were sintered to increase stability of the samples. Figure 20 presents a comparison of the color between non-sintered and sintered particles.

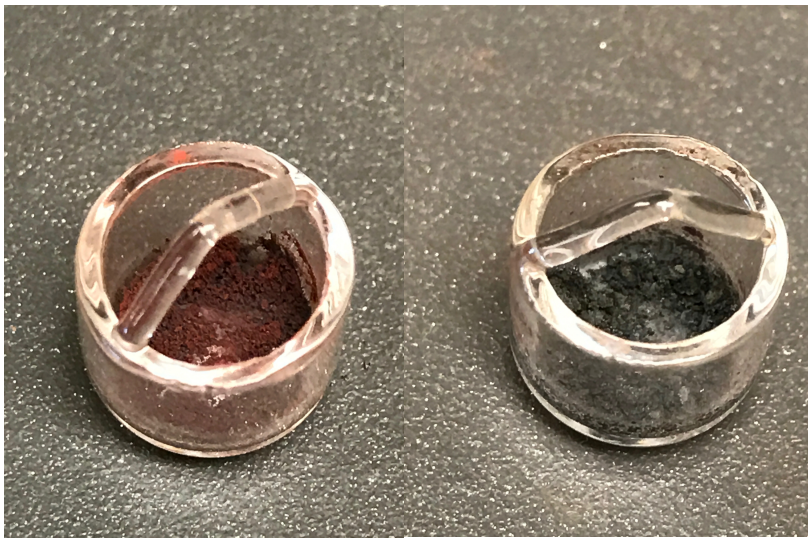

Figure 20: *Comparison of non-sintered particles (left) and sintered particles (right) prior to experimentation in the TGA.*

Particles that were not sintered appeared red while particles that were sintered had a black color. The variation in color suggests a change in the lattice density of the metals as the particles consolidate at high temperatures. Sintered particles appear darker than non-sintered particles, leading to the assumption that as the lattice structure becomes more compact light is trapped in the compound pores.

TGA Studies

Initial TGA testing was of the iron oxide control group at varying isothermal operating conditions in the TGA. Assuming that the rate of reduction by hydrogen is significantly faster than the rate of reduction by hydrogen sulfide, *equations 1 – 3* model the reduction of iron oxide [35].

$$3Fe_2O_3\ (s) + H_2\ (g) \rightarrow 2Fe_3O_4(s) + H_2O\ (g) \quad (1)$$

$$Fe_3O_4\ (s) + H_2\ (g) \rightarrow 3FeO(s) + H_2O\ (g) \quad (2)$$

$$FeO\ (s) + H_2\ (g) \rightarrow Fe(s) + H_2O\ (g) \quad (3)$$

The reduction of iron oxide particles can be characterized by three distinct stages: stage I modeled by *equation 1*, stage II modeled by *equation 2*, and stage III modeled by *equation 3*. The period of time where reduction of particles is kinetically controlled is called the reduction period, as visualized in Figure 21.

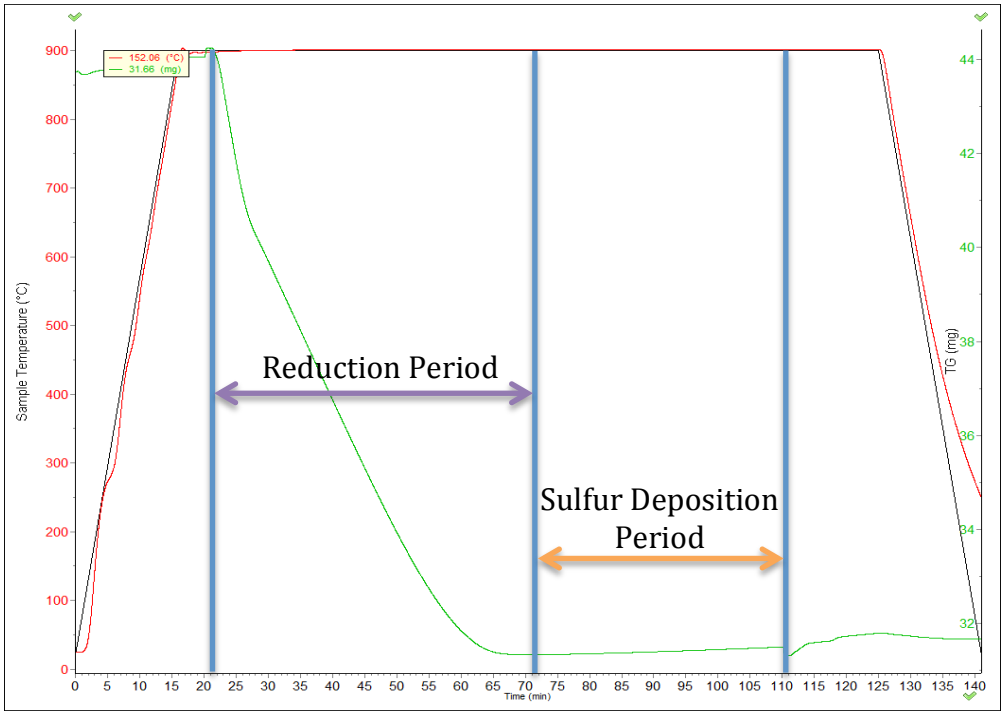

Figure 21: *Characterization of two significant reaction periods in TGA experiments. Taken from the PI (control group) experiment at 900°C.*

Once the reduction of iron oxide to iron is complete in the TGA, the reaction of iron by hydrogen sulfide takes over, as modeled by *equation 4*.

$$Fe\ (s) + H_2S\ (g) \rightarrow FeS(s) + H_2\ (g) \qquad (4)$$

The sulfur deposition period was assumed as thermodynamically controlled. Figure 21 also provides a distinction of the period of time where sulfur deposition occurs. In the sulfur deposition period there is an accumulation of sulfur on the surface of the iron particles, which can be quantified to determine the total amount of sulfur deposited after a single reduction cycle.

In the reduction period three distinct slopes are observed, each of which signify the reduction of each of the three stages outlined previously from *equations 1-3*. The rate of reaction can be quantified by measuring the average accumulation of mass over the time period inherent to the stage. The three stages are specified in Figure 22. The blue box encompasses the reduction of Fe_2O_3 in stage 1, the orange box visually represents the reduction of Fe_3O_4 in stage 2, and the purple box portrays the reduction of FeO in stage 3.

In order to determine the rate of reactions in both periods, mass balances should be considered. The system was set as the particles where the system for each stage was the metal under reduction by hydrogen gas. Taking the metal to be in a fixed location, the general batch design equation was used to model the reduction of each stage, where the iron phase at each stage is symbolized by 'A' as seen in *equation 5*.

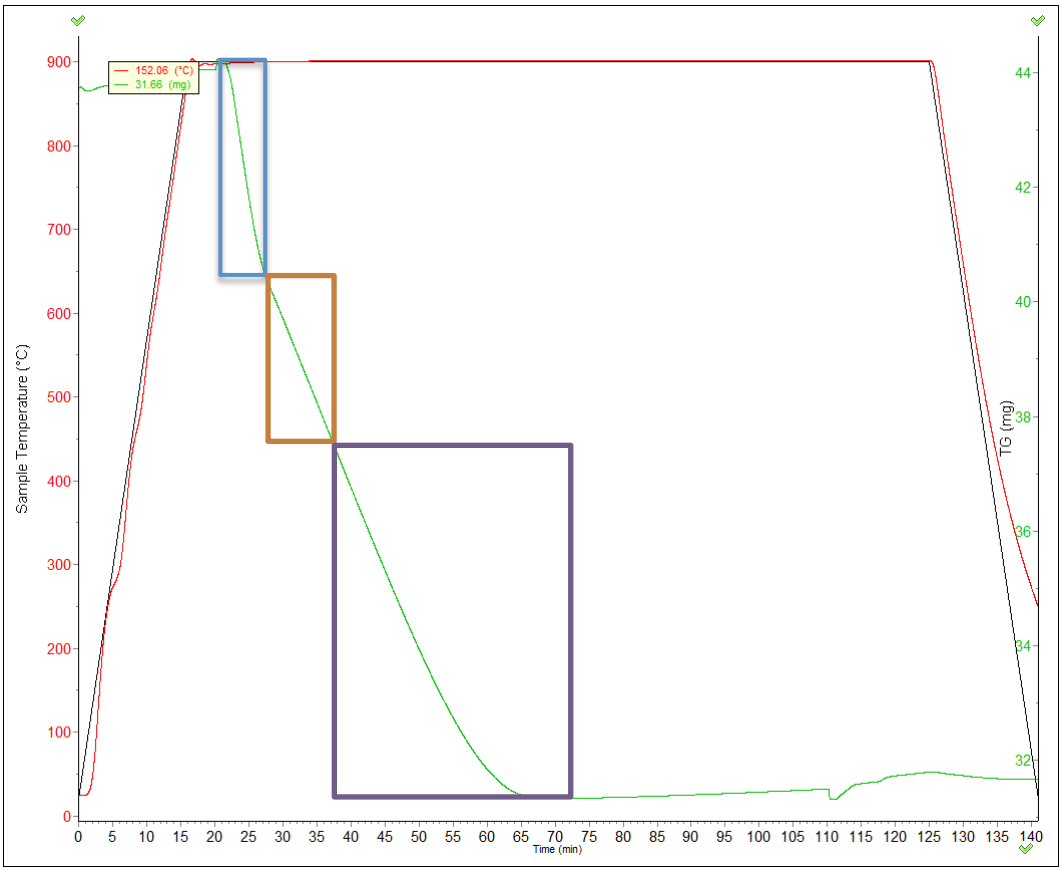

Figure 22: *Characterization of the three reduction stages in TGA experiments. Taken from the PI (control group) experiment at 900°C. Sample temperature (red line), controlled temperature (black line), and particle weight (green line) plotted over time.*

$$\frac{dN_A}{dt} = r_A V \qquad (5)$$

The accumulation term on the left hand side of the design equation was calculated by measuring the average disappearance of Fe_2O_3 by weight over the time period of reduction for stage 1. Once the change in mass over time was determined, stoichiometry was considered to calculate the total accumulation term in moles per seconds. Using *equation 5*, the accumulation term was computed on the next page where the solution was negative to account for disappearance of Fe_2O_3.

$$\frac{dN_{Fe_2O_3}}{dt} = \frac{2}{3} * \frac{dN_{Fe_3O_4}}{dt} = \frac{2}{3} * \frac{2\ mg}{2\ min} * \frac{1\ g}{1000\ mg} * \frac{1\ min}{60\ s} * \frac{1\ mole}{159.69\ g}$$

$$\boldsymbol{\frac{dN_{Fe_2O_3}}{dt} = -6.96 * 10^{-8}\ \frac{mole}{s}}$$

Rearranging *equation 5*, the rate of reaction for each phase can be determined, as postulated by *equation 6*. Taking porosity of the particles into consideration by an additional term, ϵ, the true particle volume can be considered in the calculation of the reaction rate.

$$r_A = \frac{1}{V * (1 - \epsilon)} * \frac{dN_A}{dt} \qquad (6)$$

Literature provides standard values for the theoretical volume of a crucible used for TGA experiments. Assuming a standard TGA test, the diameter of a crucible would be around 8 mm and the height of the crucible would be 7 mm [36]. Packing the cylindrical crucible to half of the total available height, the height used for calculations should be 3.5 mm. Porosity of iron oxide particles sintered in a resistive furnace has a average value, obtained from literature, of 0.104 [36]. Weight of the particles loaded into the TGA could be used in replacement of particle volume. The researcher assumed that a constant volume assumption would be more accurate in modeling the study as the effective weight of particles vary with reaction time.

The computation of the rate of reaction for Fe_2O_3 in stage 1 of the reduction period is performed below and is continued at the beginning of the next page.

$$r_{Fe_2O_3} = \frac{1}{V * (1 - \epsilon)} * \frac{dN_{Fe_2O_3}}{dt}$$

$$r_{Fe_2O_3} = \frac{1}{(\pi * (\frac{8\ mm}{1} * \frac{1\ m}{1000\ mm})^2 (\frac{3.5\ mm}{1} * \frac{1\ m}{1000\ mm})(1 - 0.104)} * -6.96 * 10^{-8}\ \frac{mole}{s}$$

$$\boldsymbol{-r_{Fe_2O_3}} = \frac{1}{6.305 * 10^{-7}\ m^3} 6.96 * 10^{-8}\ \frac{mole}{s} = \boldsymbol{0.11\ \frac{mole}{m^3 * s}}$$

Figures A1, A2, and A3 in *Appendix A* reveal the reduction of control group over time at 700ºC, 800ºC, and 900ºC respectively. Qualitatively, it can be visualized in these plots that as the TGA operation temperature increases the slopes for each of the three phases becomes steeper. This change in slope suggests that the reduction of iron oxide is largely dependent on temperature.

Analyzing Figures A1, A2, and A3, in *Appendix A,* the rate of reaction was determined for each of the three stages. Following the same process explored previously in the determination of $-r_{Fe_2O_3}$ at 900ºC; the calculated rates of reaction are provided in Table 5. Special care was taken in adjusting the stoichiometric ratios and molecular weights from stage to stage, as each stage modeled the reduction of a different phase of iron. It was found in Table 5 that the fastest reaction occurred in the reduction of Fe_2O_3 to Fe_3O_4, which is to be expected from use of H_2, which acts as a strong reducing agent.

Table 5: *Rates of reduction in the control group at various reactor temperatures.*

	700ºC	**800ºC**	**900ºC**
Stage 1 ($-r_{Fe_2O_3}$)	$0.065\ \frac{mole}{m^3 * s}$	$0.071\ \frac{mole}{m^3 * s}$	$0.110\ \frac{mole}{m^3 * s}$
Stage 2 ($-r_{Fe_3O_4}$)	$0.054\ \frac{mole}{m^3 * s}$	$0.066\ \frac{mole}{m^3 * s}$	$0.103\ \frac{mole}{m^3 * s}$
Stage 3 ($-r_{FeO}$)	$0.033\ \frac{mole}{m^3 * s}$	$0.049\ \frac{mole}{m^3 * s}$	$0.053\ \frac{mole}{m^3 * s}$

Analyzing the data in Table 5, clear quantitative trends are formed. In agreement with the qualitative analysis made of Figures A1, A2, and A3, in *Appendix A*, the rate of reduction for each stage increased with increasing temperature. Stage 2 of the reduction period was the most ambiguous to identify qualitatively. Challenges in the determination of a discrete time period for stage 2 led to the highest opportunity for error when propagating the rate of reduction calculations. It should be noted that rates of disappearance term for each stage is negative due to the loss of weight for that particular phase of iron over the course of the reaction.

The rate of formation for iron-sulfide bonds in the sulfur deposition period can be determined by following the approach used for the calculations of rate of reaction in the reduction period. For the control group, PI, it is clear that the only accumulation that occurs is by iron-sulfide bonds. Utilizing the stoichiometric ratio of the metals in *equation 4*, the rate of formation of iron-sulfide, r_{FeS}, can be determined at each temperature. The calculated rates of formation for the control group are tabulated in Table 6.

Table 6: *Rates of formation in the control group at various reactor temperatures.*

	700°C	**800°C**	**900°C**
Rate of Formation (r_{FeS})	N/A	$8.27 * 10^{-4} \frac{mole}{m^3 * s}$	$2.10 * 10^{-3} \frac{mole}{m^3 * s}$

Special care was taken in the adjustment of the stoichiometric ratio and the molecular weight from the equations used in the reduction period to the sulfur deposition period. Just as in Table 5, the rate of formation for iron-sulfide bonds

increased with increasing TGA operation temperatures. It should be noted that the rate of formation was not calculated for trials tested at 700ºC due to experimental error that led to an incomplete reaction time.

Once the control group was thoroughly studied, the researcher formed binary phase particles with various ratios, by weight, of molybdenum oxide to iron oxide. Once sintered, the particles were reacted in the TGA and an analysis was performed for two different isothermal temperature conditions: 800ºC, and 900ºC. Due to limitations in the ability for the researcher to study the rates of reaction of the binary phase particles with kinetic models, the focus of this section is strictly in the analysis of the sulfur deposition period. Figure 23 plots the reduction period and sulfur deposition period for particle PIIa.i at 900ºC.

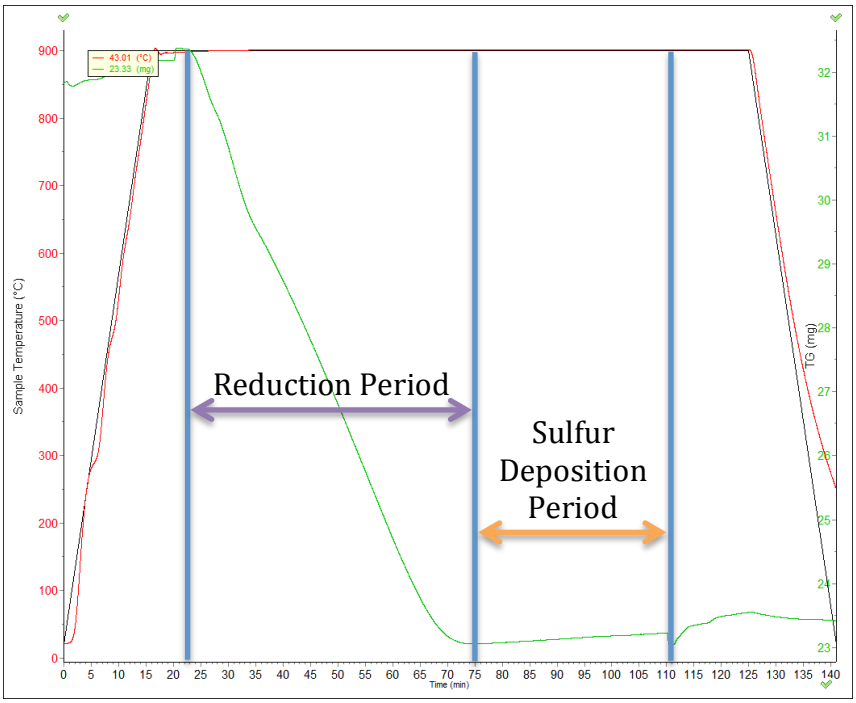

Figure 23: *Characterization of both the reduction period and sulfur deposition period for particle PIIa.i at 900ºC.*

The rate of formation for iron-sulfide bonds in the sulfur deposition period can be determined by following a similar approach used for the calculations of rate of formation for the control group. As will be discussed in the *XRD Studies* section, for each experimental group it is clear that sulfur accumulation occurs on both the iron phase and the molybdenum phase. Figures A4-A12, in *Appendix A*, plot TGA data for iron and molybdenum mixtures at reactor conditions of 700ºC, 800ºC, and 900ºC.

Assuming that the sintered particles form a binary phase of iron and molybdenum, the bulk density of the particles is a ratio of the total mass to the bulk volume. Scaling the weight of the particles, with respect to the weight ratio of the two metals, allows for the engineer to assume that the volume of the particles scales directly. For simplicity, it was assumed that all sulfur deposited only on active sites of iron to form iron-sulfide bonds. The calculated rates of formation for iron-sulfide are plotted against isothermal reaction temperatures of 800ºC and 900ºC in Figure 24.

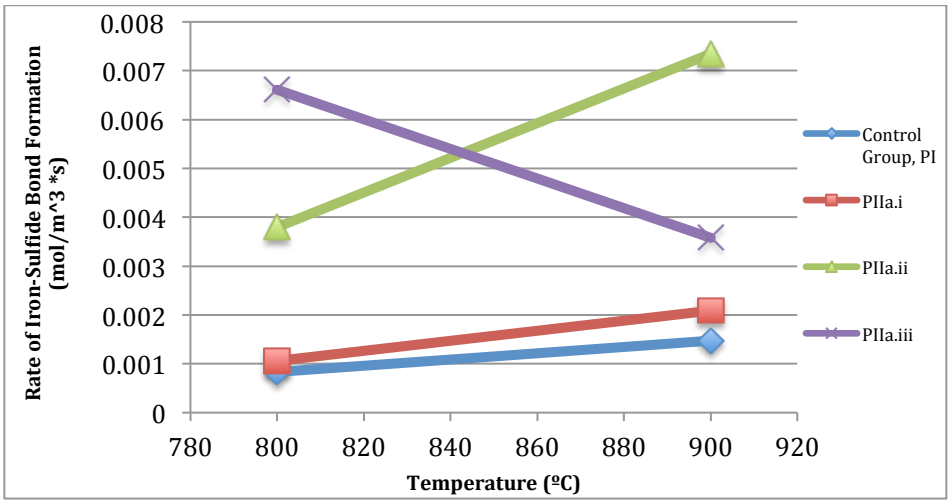

Figure 24: *Rates of iron-sulfide formation against reactor temperature.*

Molybdenum active sites were assumed to be the most significant contributor to the deposition of sulfur on the surface of the oxygen carrier due to an analysis of the data collected by XRD studies. This assumption will be explored more in the *XRD Studies* sub-section of this report. The most notable trend in Figure 24 is that as the isothermal reactor temperature increases in the TGA, the rate of iron-sulfide formation also increases. The 1:1 weight ratio of iron to molybdenum follows an opposite trend. While various attempts were made to replicate the study, the researcher was not able to obtain new data points to refute the collected data for PIIa.iii particles in the time period given to accomplish this thesis study. These data points will be omitted from further examination in this section. Figure 25 highlights the trends inherent to the data points of significance.

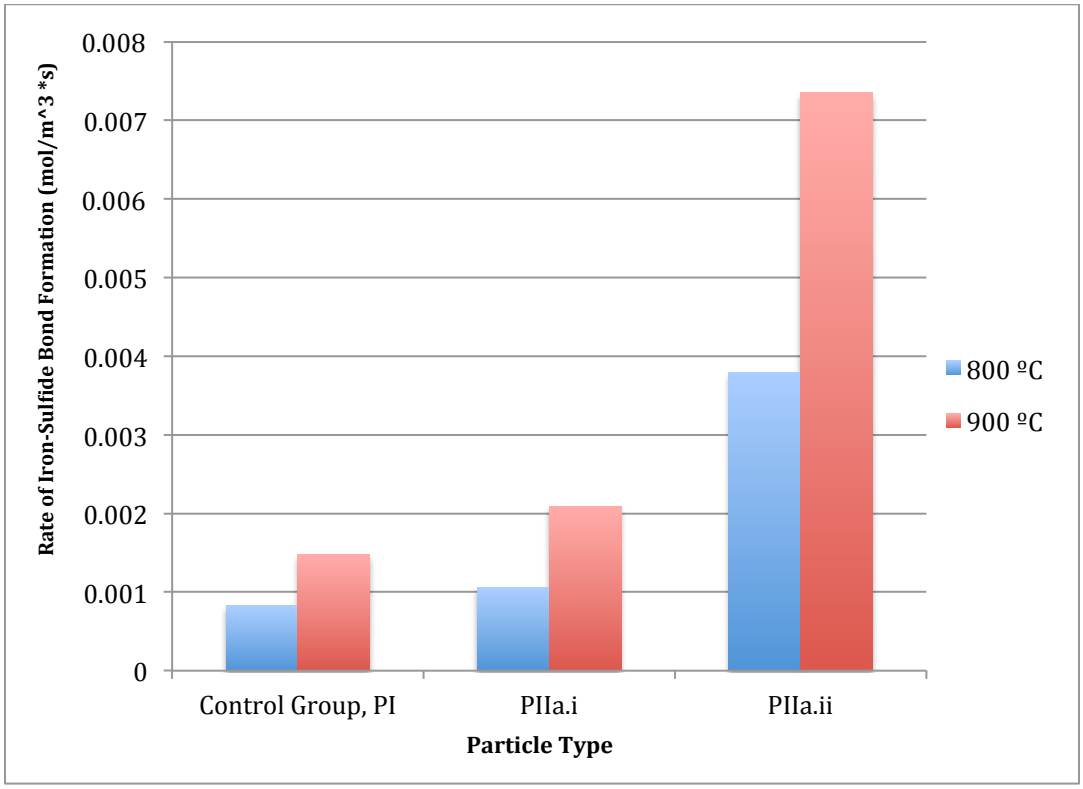

Figure 25: *Comparison of the rate of iron-sulfide formation based on reaction temperature for various particles.*

For the compounds of interest, there is a clear trend in Figure 25 suggesting that with increasing molybdenum content there is an increase in the rate of sulfur deposition. This trend is significant as literature argues that the formation of iron-sulfide bonds should decrease with an increase in molybdenum content due to the hydrodesulfurization (HDS) mechanism of molybdenum. HDS mechanisms support the notion that the molybdenum active site is more appealing for sulfur deposition in comparison to active sites of iron.

Figure 25 portrays rates of metal-sulfur bond formation. In studying the rate of sulfur deposition, it was assumed that all hydrogen sulfide introduced to the system formed iron-sulfide scale. As will be discussed further in the *XRD Studies* section, molybdenum-sulfide bonds formed in addition to iron-sulfide bonds. The formation of sulfur scale on particles is expected from a thermodynamic analysis.

The Gibbs free energy of formation associated with the formation of iron-sulfide and molybdenum-sulfide bonds aids the researcher in the determination of which bond is expected to be the predominant product formed on the surface of the particles. Table 7 presets the standard Gibbs free energy of formation values determined for iron-sulfide and molybdenum-sulfide phases at standard conditions of 1 atmosphere and 25ºC.

Table 7: *Standard Gibbs free energy of formation [37] [38].*

Iron (II)-Sulfide	Molybdenum (IV)-Sulfide
ΔG_f^o (s): -100.42 kJ/mol	ΔG_f^o (s): -225.94 kJ/mol

Negative values of Gibbs free energy represent a spontaneous formation of compounds, while a Gibbs free energy value of zero denotes that the system has reached a chemical equilibrium. Due to limitations in data collected from a literature review, thermodynamic properties of these formed bonds of iron-sulfide and molybdenum-sulfide could not be obtained. At standard conditions, Table 7 suggests that the sulfur deposition is favorable. Non-standard condition calculations were outside of the abilities of the researcher, so a standard condition basis was chosen. Applying a thermodynamic perspective to these data collected by TGA experimentation, it can be confirmed that the reactor conditions were favorable to allow the deposition of sulfur.

With an increase in 100ºC between the 800ºC trials and the 900ºC trials, the rate of sulfur deposition approximately doubled, as visualized in Figure 25. From a kinetic perspective, an increase in the rate of reaction is expected as the number of interactions between the metal surface and the hydrogen sulfide gas should increase with an accompanied increase in temperature.

The large jump in the rate of reaction from the PIIa.i to the PIIa.ii phase is observed to occur in the same ratio between the 800ºC and 900ºC trials. The observed quadratic nature of these data suggests that molybdenum does in fact play a substantial role in sulfur deposition. Due to the large magnitude of increase in the rate of metal-sulfide bond formation with an increase in the ratio of molybdenum present in the particles, it can be argued that the presence of molybdenum increases the rate of sulfur deposition. Furthermore, the

molybdenum phase can be proposed to more selectively adsorb sulfur under the tested reactor conditions in comparison to the iron phase.

XRD Studies

The XRD was utilized to characterize the specific phases observed for each particle, both before and after reaction in the TGA. In the TGA Studies section, the researcher assumed that all sulfur deposition occurred on the surface of iron and not on the surface of molybdenum for simplicity in calculations. This assumption was made to provide a surface-level analysis of the effects of both temperature and composition on the rate of sulfur deposition for the particles. Using data collected from powder XRD experimentation, one can suggest phases present in the particles.

A fast scan was performed on each sample in the XRD to highlight peaks of interest that could aid the researcher in the characterization of various phases. Figure 26 portrays the measured intensity in counts per second against the double angle by which the instrument studied the specimen. All peaks above 75 degrees were discounted by recommendation of graduate students in the research team. Intense peaks were identified in Figure 26 to further examine by increasing the time scale required to scan the specimen. These peaks were grouped into areas of interest, as visualized by the green, red, and purple braces and arrows.

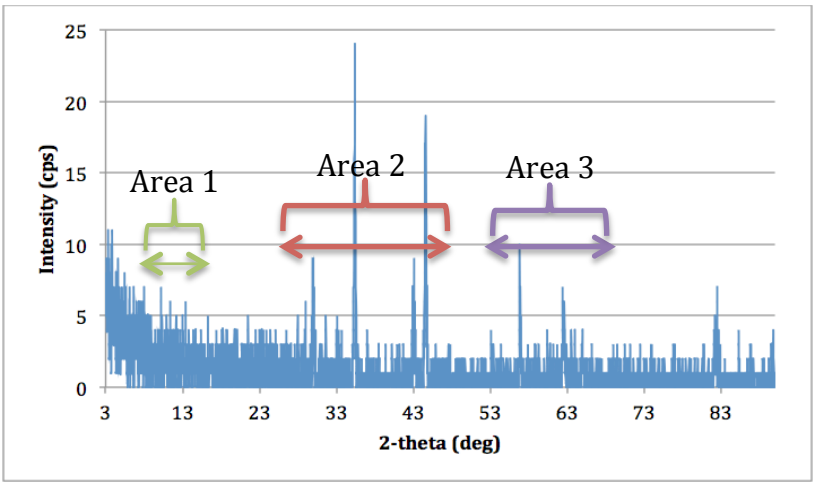

Figure 26: *Quick study characterization of particle PIIa.i at 900ºC taken at 4 degrees per minute. Three distinct areas of interest are identified.*

Due to initial time constraints, Area 1 was initially omitted from an in-depth study to allow the researcher the opportunity to thoroughly study Areas 2 and 3. Figure 27 explores the areas of interest by scanning the specimen at a rate of 0.25 degrees per minute – a 1500% increase in time from the fast scan.

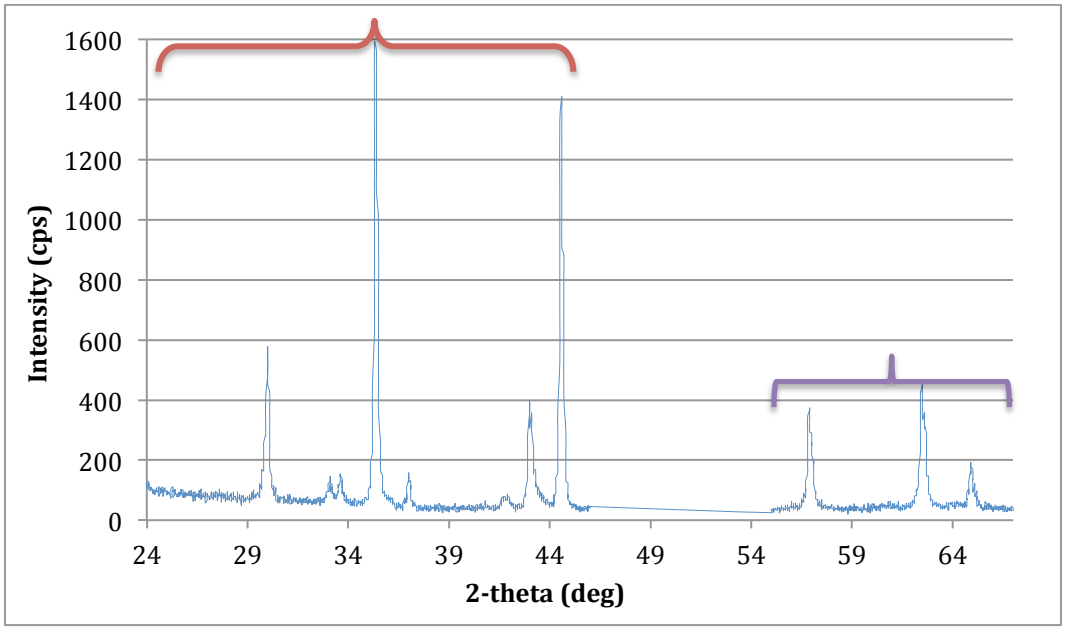

Figure 27: *Characterization of particle PIIa.i at 900ºC taken at 0.25 degrees per minute. Area 2 is shown by the red brace. Area 3 is shown by the purple brace.*

Using the data acquisition tool software, provided by the computer running the powder XRD instrument, the peaks were characterized. By matching the peaks observed to peak patterns from literature, one could strongly suggest the emergence of possible phases in the specimen. Figure 28 is a reference plot of intensities that should appear in a specimen with a present iron-oxide phase. Comparing the relative intensity peaks in Figure 28 to the peaks observed in Figure 27, one can justify that an iron-oxide phase has the potential to exist.

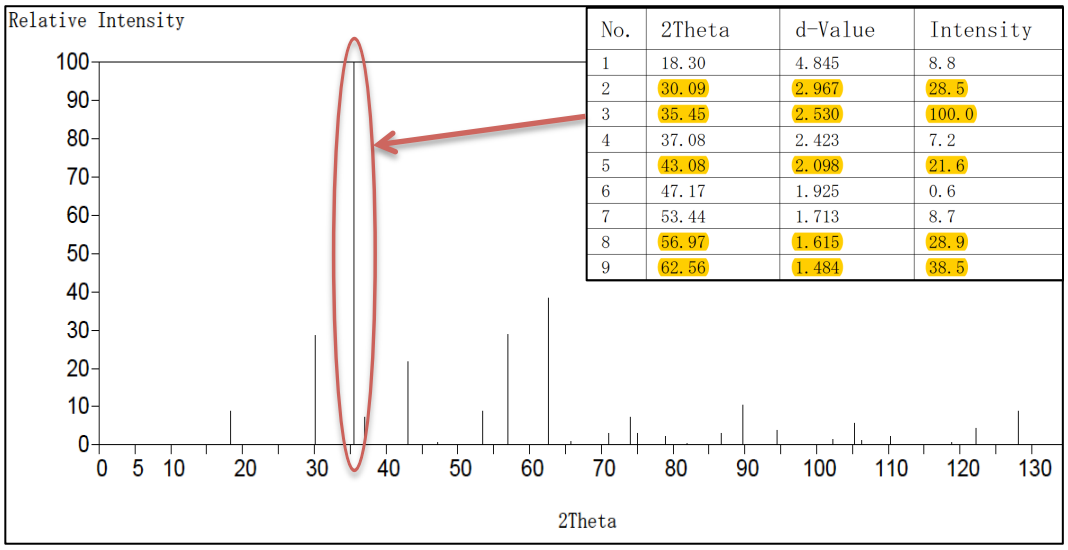

No.	2Theta	d-Value	Intensity
1	18.30	4.845	8.8
2	30.09	2.967	28.5
3	35.45	2.530	100.0
4	37.08	2.423	7.2
5	43.08	2.098	21.6
6	47.17	1.925	0.6
7	53.44	1.713	8.7
8	56.97	1.615	28.9
9	62.56	1.484	38.5

Figure 28: *Reference peaks used to characterize an iron-oxide (Fe_3O_4) phase.*

Before stating that a phase exists in a specimen, it is important to consider relative phases that could also exist in order to avoid incorrectly characterizing particles. Figure 28 works to identify a specific peak that appears to exist in Figure 27 by the addition of a red ellipsis at a 2-theta value of 34.45 degrees. Upon further evaluation with various iron phases from literature, the researcher concluded that this peak of high intensity inherent to Figure 26 was actually characterized by standard iron, Fe.

Iron-sulfide bond formation can be justified by characterizing iron-sulfide phases of specimen in powder XRD experiments. Studying Area 2 of Figure 26, one observes various peaks of significance. Figure 29 magnifies the scale used to visualize these peaks so that peaks with less relative intensity can be explored.

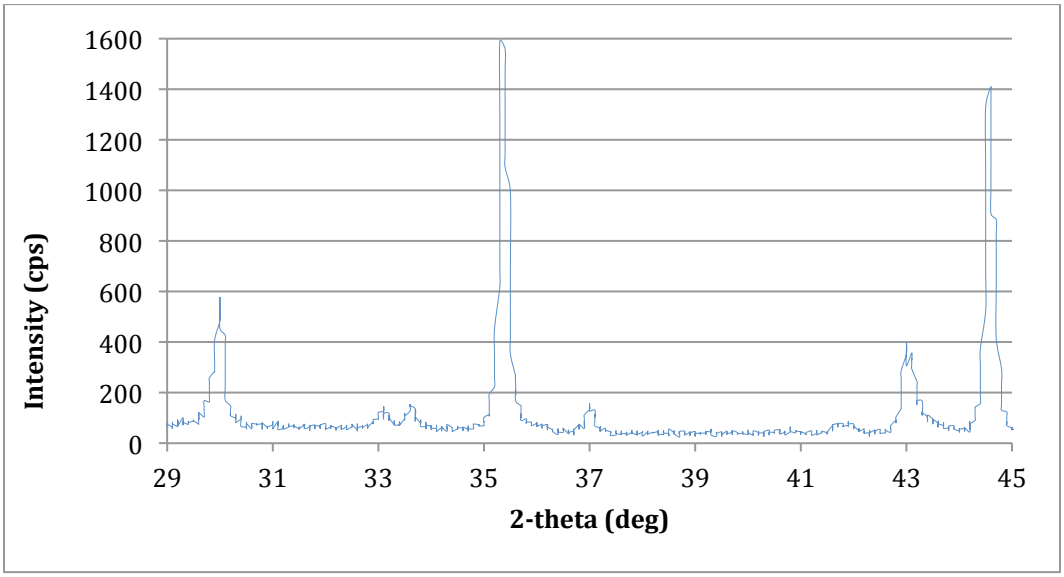

Figure 29: *Characterization of Area 2 in particle PIIa.i at 900ºC.*

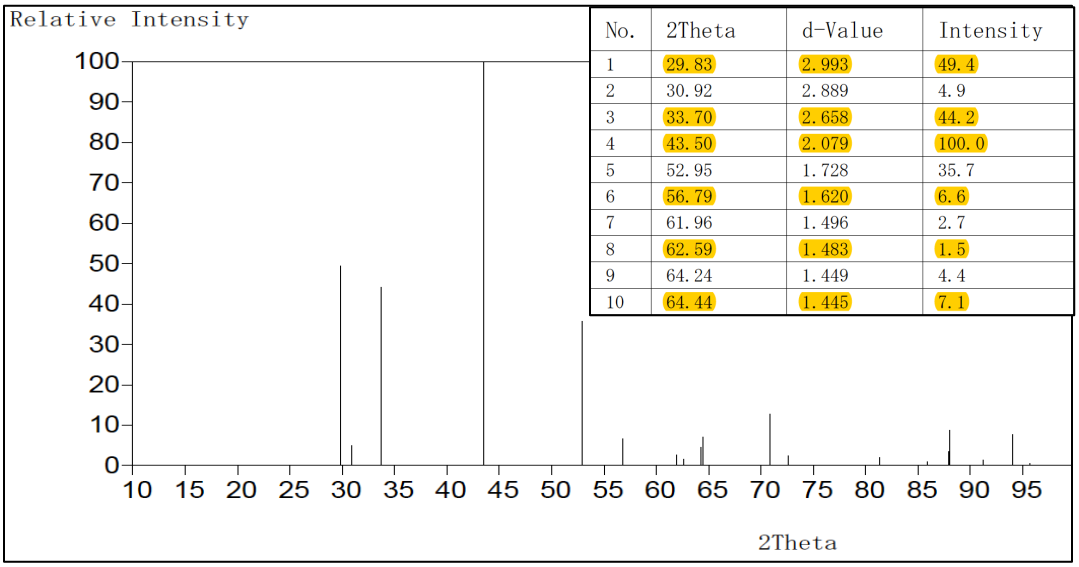

No.	2Theta	d-Value	Intensity
1	29.83	2.993	49.4
2	30.92	2.889	4.9
3	33.70	2.658	44.2
4	43.50	2.079	100.0
5	52.95	1.728	35.7
6	56.79	1.620	6.6
7	61.96	1.496	2.7
8	62.59	1.483	1.5
9	64.24	1.449	4.4
10	64.44	1.445	7.1

Figure 30: *Reference peaks used to characterize an iron-sulfide (Fe-S) phase.*

Comparing various generated phase references to Figure 29, the researcher recognized that the peaks at 2-theta values of 29.83 and 33.70 were distinct. These peaks only matched those of an iron-sulfide phase. Additionally, matching the peaks at 2-theta values of 56.79 and 62.59 degrees in Figure 31 to the reference peaks in Figure 30, one sees matching peaks of intensity that could suggest the presence of an iron-sulfide phase.

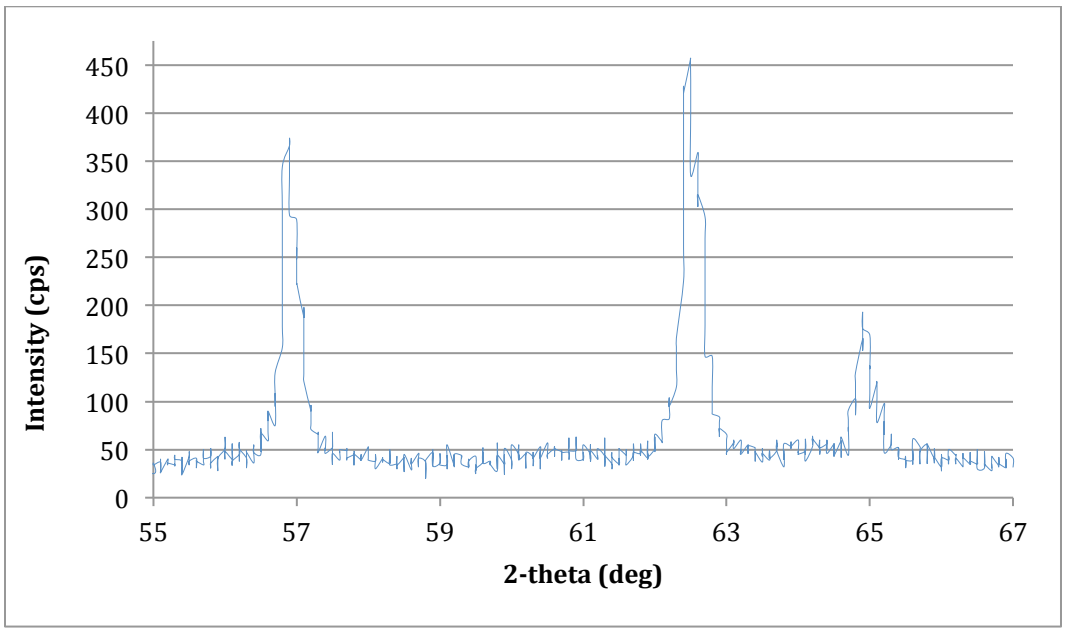

Figure 31: *Characterization of Area 3 in particle PIIa.i at 900ºC.*

In several of these peaks, such as that at a 2-theta value of approximately 65 degrees in Figure 31, one observes a non-smooth peak. Non-symmetrical peaks indicate two possibilities: noise in the reading that can be eliminated by running a scan of the specimen for a longer period of time, or various peaks in a shared area. In the event that various peaks share a similar area, it is likely that those peaks all share common element, such as Fe, and differ based on various additional elements bonded to the shared element. For example, it is common to see Fe_2O_3 and Fe_3O_4 share similar 2-theta values, making the utilization of reference

literature vital in order to properly characterize metal phases when using the powder XRD instrument. In both Figures 29 and 31, these distinct peaks strongly suggest the presence of iron-sulfide in particle PIIa.i run at 900ºC. Studying the other trials tested in the XRD, found in *Appendix B*, it can be concluded that the iron-sulfide phase was present in all tested particles.

Examining the trials in search for a molybdenum-sulfide peak, these data initially revealed a small, if not insignificant, presence of a molybdenum-sulfide phase. Investigating Area 1 of Figure 26, the researcher noticed a difference at a 2-theta value around 13.5 degrees between the control group and the area in Figure 26. Magnifying the perspective, Figure 32 portrays a peak of significance, circled in red, which exists for all trials that contain molybdenum. This peak suggests the presence of molybdenum and explores the opportunity to visualize a molybdenum-sulfide phase.

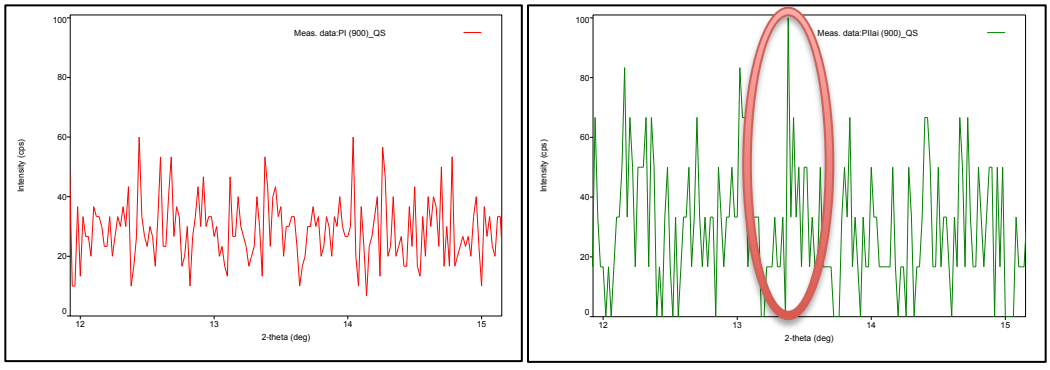

Figure 32: *Characterization of particle PI at 900ºC (on the left) and particle PIIa.i at 900ºC (on the right).*

Analyzing the data collected for all specimens at this region, peaks of interest are observed. Using the software provided, reference peaks are matched with the

peaks of interest. Investigating several possible phases that could represent the peak at a 2-theta of about 13.5 degrees, the researcher ultimately determined that the phase best matched that which was referenced as a molybdenum-sulfide (Mo-S) phase. The reference peak for Mo-S is shown as a green line in Figure 33.

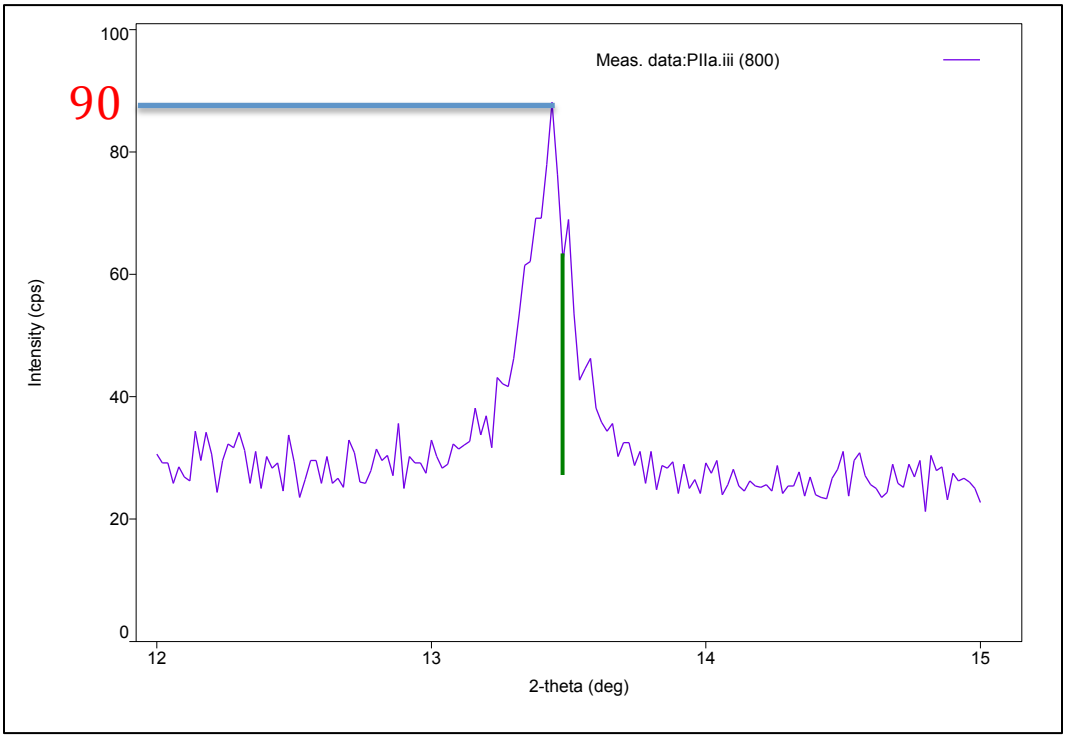

Figure 33: *Characterization of molybdenum-sulfide (MoS2) for PIIa.iii at 800ºC.*

In particle PIIa.iii the researcher observed the most distinct peaks in the 2-theta region between 12 and 15 degrees, suggesting that the increased composition of molybdenum in the particles influenced the ability for the instrument to detect molybdenum phases in specimen. Furthermore, comparing the intensity of the peaks at a 2-theta value of 13.5 degrees for particle PIIa.i in Figure 34 to that for particle PIIa.iii one observes that the peak intensity roughly doubles in magnitude. The addition of blue lines in both Figures 33 and 34 aids the researcher in making rough estimates of the peak intensities.

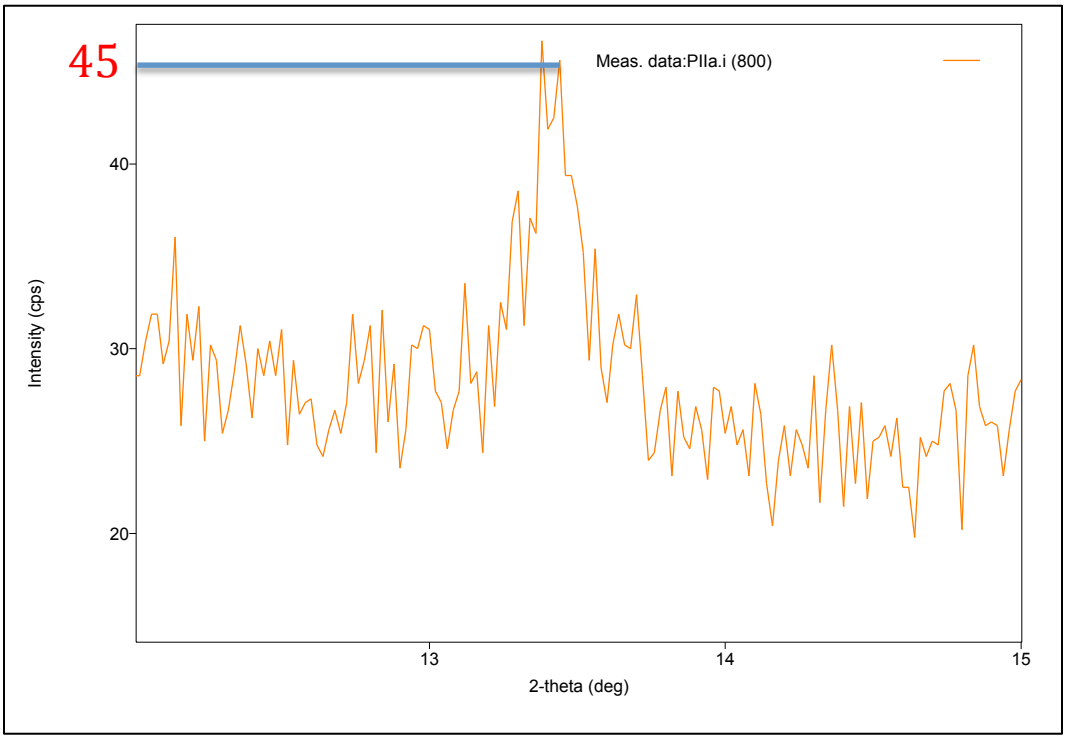

Figure 34: *Characterization of molybdenum-sulfide (MoS2) for PIIa.i at 800ºC.*

Both trials, taken from particles that were tested at 800ºC, showed two significant peaks at a 2-theta value of about 13.5 degrees. The increase in the magnitude of the intensity for the distinct peak of a molybdenum-sulfide phase suggests that with an increased concentration of molybdenum in the particle, there was a greater area of molybdenum on which for sulfur to deposit. With an increase in the number of molybdenum active sites, this would suggest that there should be a proportional increase in the rate of reaction for the formation of molybdenum-sulfur bonds.

These data propose that there is a significant presence of the molybdenum-sulfide phase for all trials. Additionally, these data suggest an increase in the formation of molybdenum-sulfide bonds with an increased composition of molybdenum.

Conclusion

Summary

Within chemical looping, a dual circulating fluidized bed is utilized to induce the carriage of oxygen from the combustor to the reducer. CDCL processes drive the reactions involved in combustion and work to decrease the rate of production of hazardous air pollutants normally produced within combustion reactions. An example of this is the elimination of as nitrous oxides (NO_x) as byproducts of coal-fired power plant operations.

Due to an increase in the utilization of bituminous coal for power plant operations, oxygen carriers must be modified on the molecular level as to increase the toleration of high sulfur content coal. One can expect an extended lifespan of the metal-oxygen carrier particles for CDCL processes once the iron phase in the particles develops a tolerance to poisoning. Furthermore, it is desirable for the modification of the metal oxygen carrier to improve process performance and diminish pollution from the operation.

Molybdenum was proposed as a metal additive to the makeup of the metal oxygen carriers utilized in current CDCL processes. Literature postulates that molybdenum possesses the ability to selectively accept sulfur atoms through mechanisms of hydrodesulfurization. In order for molybdenum to be a competitive additive in the make up of metal oxygen carriers, molybdenum

needed to show characteristics of a strong sulfur accepter at similar operating conditions to those encountered in the oxy-combustion stage of a CDCL process.

With an increase in the ratio of molybdenum in the makeup of the particles, there was an observed proportional increase in the deposition of sulfur. XRD studies suggested that with an increase in ratio of molybdenum, there was an increase in the presence of a molybdenum-sulfide phase. These data suggest that by allowing molybdenum to act as a collector of sulfur volatiles, the iron phase of the oxygen carrier can continue transporting oxygen from the combustor to the reducer with a lessened interference of sulfur by mechanisms of sulfur poisoning.

The environmental impacts of adsorbing sulfur to the surface of iron or molybdenum are currently unknown. It is suggested that the sulfur would either burn off of the particles in the combustor or remain on the particles throughout experimentation in the CDCL process. By burning off the sulfur from the metal surface in the combustor, an increase in air pollution control equipment would be necessary so that EPA standards can be followed. This addition is currently costly to a company that implements CDCL technology. With future knowledge and experimentation, this can be studied so that the economics performance of the process can be optimized.

Future Work and Recommendations

A shortcoming within this study will be having ample time to thoroughly analyze data on characteristics of iron and molybdenum phases after reduction. Future

testing should focus on the application of additional instruments, the optimization of metal oxygen carrier performance, and collaborating with other teams to take a computational approach to the study.

The scanning electron microscope (SEM) instrument provides a valuable perspective of the particles by analyzing the metal surface morphology. Using the SEM, a high-resolution image can be taken to aid in the collection of data for catalysis, pharmaceuticals, and material science research. The SEM can be applied to this study to observe surface deformation of the metal oxygen carriers from sulfur poisoning in the TGA experiment.

Using an electron gun, beams of electrons are projected through a series of magnetic propulsion stages that detect the specific wavelengths of electrons before striking the surface of the particles. Once the electrons are ejected from the surface of the particle, a secondary electron detector is used in comparison to the initial electron detector to ultimately form an image through manipulation of the wavelengths. By striking the surface with minimal penetration of the specimen, information of the surface morphology for the specimen can be obtained.

Sputter coating was incorporated in order to maintain the charge of specimen stuck by electrons. Sputter coating is a process by which an ultra-thin layer of gold is applied to the surface of the specimen [39]. By operating the instrument in a vacuum, the researcher decreases the opportunity for air molecules to disrupt the pathway of the electron beam and ultimately a sharp image can be obtained. A

graphic depicting the process utilized in the SEM instrument can be found in Figure 35.

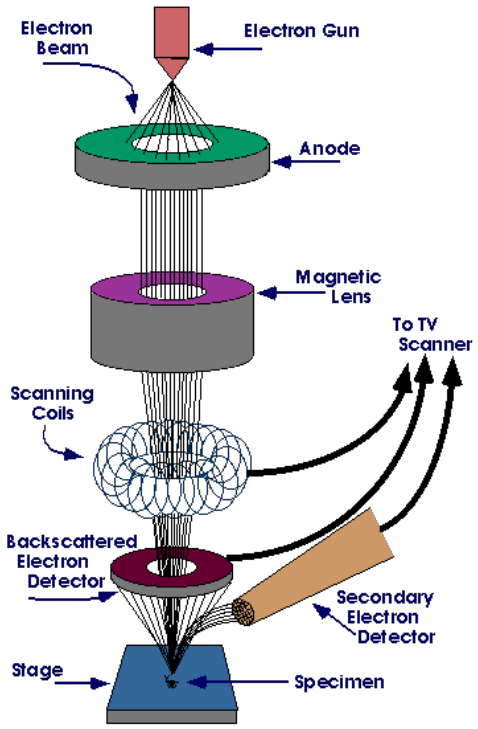

Figure 35: *SEM process [40].*

In future research, it would be effective to study simulations of iron-sulfide bond formation on particles with other common support in CDCL process, such as Al_2O_3 and TiO_2. Iron oxide is not the only chemical used in industrial metal oxygen carriers, leading to the use of various support chemicals to improve performance.

Literature suggests that other metals, such as boron, could follow similar desulfurization mechanisms to molybdenum [18]. In future studies, it would be favorable to optimize the performance of metal oxygen carriers by varying the ratio of Fe_2O_3 to the ratios of support materials and metal additives, such as

molybdenum and boron [9]. Possible environmental, health, and safety hazards should be further invested in the event that molybdenum and boron are integrated into the make up of metal oxygen carriers.

Calculations can be performed to estimate the Thiele modulus and internal effectiveness factor inherent to sulfur deposition. These parameters aid the researcher in determining if the mechanism for sulfur deposition is reaction rate limited or internal diffusion limited. Considering the mass transfer within the column could allow for the determination of the efficiency of sulfur deposition at various reactor conditions. This can ultimately be used to optimize the concentration weight ratio of molybdenum to increase particle sulfur tolerance.

It would be ideal to collaborate with other researchers in the Fan laboratory with experience in computational catalysis so that the mechanisms inherent to this formation of iron-sulfide and molybdenum-sulfide bonds could be studied. By using computational methods, more complicated kinetic studies can be performed in studying the rate of reaction in both the reduction period and the sulfur deposition period. Once the mechanisms are better understood, one can integrate data collected from the instruments with material balances to determine a more accurate ratio of iron-sulfide bonds to molybdenum-sulfide bonds formed in TGA experiments.

References

[1] EPA. "Annual Energy Outlook 2015." Environmental Protection Agency, 2015.

[2] EPA. "Clean Power Plan for Existing Power Plants." Environmental Protection Agency, 2016.

[3] EPA. "Summary of the Nuclear Waste Policy Act." Environmental Protection Agency, 08 Sept. 2016.

[4] Fan, Liang-Shih. *Chemical Looping Systems for Fossil Energy Conversions*. Hoboken, NJ: Wiley- AIChE, 2010.

[5] The Effect of Coal Volatility on Mercury Removal from Bituminous Coal during Mild Pyrolysis. "The Effect of Coal Volatility on Mercury Removal from Bituminous Coal during Mild Pyrolysis." [Accessed 17 February 2017].

[6] Miners Museum Glace Bay Nova Scotia Canada. "Miners Museum - Cape Breton." [Accessed 17 February 2017].

[7] Governor Ted Strickland, Ohio State Department Of Natural Resources. *GEOLOGY OF COAL.* [Accessed 12 February 2017].

[8] SpringerReference. "Sulfur Emissions and Midwest Power Plants." [Accessed 12 February 2017].

[9] Approved Code of Practice for the Prevention of Sulphur Fires and Explosions. Wellington, N.Z.: Occupational Safety &

Health Service, Dept. of Labour, 1993.

[10] Union of Concerned Scientists. "The Clean Air Act." [Accessed 5 February 2017].

[11] Air Quality Index (AQI) Basics. "Air Quality Index (AQI) Basics." [Accessed 5 February 2017].

[12] EPA "Chemical-looping-combustion | Netl.doe.gov." *Chemical-looping-combustion | Netl.doe.gov*, 2016.

[13] Solunke, Rahul D. and Veser, Gotz. "Integrating desulfurization with CO_2-capture in chemical-looping combustion". [Accessed 17 February 2017].

[14] Adanez, Juan. "Progress in Chemical-Looping Combustion and Reforming technologies". [Accessed 15 February 2017].

[15] "Integrating Desulfurization with Molybdenum." *Integrating Desulfurization with CO2-capture in Chemical-looping Combustion*. [Accessed 12 February 2017].

[16] ResearchGate. "Mechanism of Catalyst Deactivation." [Accessed 15 February 2017].

[17] Kunii, Daizo and Levenspiel, Octave. *Fluidization Engineering.* Butterworth-Heinemann, 2009

[18] Van Ommen, Ruud J. and Ellis, Naoko "Fluidization" [Accessed 12 February 2017].

[19] Grace, John R.; Leckner, Bo; Zhu, Jesse; Cheng, Yi (2008), "Fluidized Beds", in Clayton T. Crow, *Multiphase Flow Handbook*, CRC Press, p. 5:71, doi:10.1201/9781420040470.ch5, ISBN 978-1-4200-4047-0. [Accessed 5 February 2017].

[20] ACS. "First Commercial Fluid Bed Reactor". *National Historic Chemical Landmarks*. [Accessed 17 February 2017].

[22] EIA. “U.S. Downstream Processing of Fresh Feed Input by Catalytic Cracking Units” (Energy Information Administration, U.S. Dept. of Energy). [Accessed 17 February 2017].

[22] Thermopedia, “Fluidized Bed” http://www.thermopedia.com/content/46/ [Accessed 12 February 2017].

[23] Weimer, “Fluidized Bed Reactor Processes” [Accessed 6 February 2017].

[24] Geankoplis, Christie J. *Transport Processes and Separation Process Principles: (includes Unit Operations)*. Upper Saddle River, NJ: Prentice Hall Professional Technical Reference, pg. 120-121, 2009

[25] Unpublished data. [Accessed 5 February 2016].

[26] The Adsorption and Reactions of Hydrocarbons on Molybdenum Single Crystal Structures. "The Adsorption and Reactions of Hydrocarbons on Molybdenum Single Crystal Surfaces; When in the Presence of Co-adsorbed Sulfur or Carbon.” *When Clean and in the Presence of Co-Adsorbed Sulfur or Carob.* [Accessed 8 February 2017].

[27] ResearchGate. "Iron-molybdenum-oxide Catalysts for Selective Oxidation of Hydrogen Sulfide to Sulfur." [Accessed 7 February 2017].

[28] Powder. "Molybdenum." [Accessed 7 February 2017].

[29] *Integrating Desulfurization with CO2-capture in Chemical-looping Combustion*. "Integrating Desulfurization with Molybdenum." [Accessed 7 February 2017].

[30] Eni Generalic, Faculty of Chemistry and Technology, Split, Croatia. "CHEMISTRY GLOSSARY." Ball+mill @ Chemistry Dictionary & Glossary. [Accessed 11 February 2017].

[31] ResearchGate. "Iron-molybdenum-oxide Catalysts for Selective Oxidation of Hydrogen Sulfide to Sulfur." [Accessed 17 February 2017].

[32] Techniques. "X-ray Powder Diffraction (XRD)." N.p., 10 Nov. 2016.

[33] Bragg Peaks. "Credo.ttk.mta.hu Creative Research Equipment for Diffraction." [Accessed 12 February 2017].

[34] The Mechanism of Reduction of Iron Oxide by Hydrogen. "The Mechanism of Reduction of Iron Oxide by Hydrogen." [Accessed 12 February 2017].

[35] Dictionary of Polymers. "Thermogravimetric Analysis (TGA)." Encyclopedic Dictionary of Polymers, 1973.

[36] Comparative Study of Porosity and Pores Morphology. "Comparative Study of Porosity and Pores Morphology of Unalloyed Iron Sintered in Furnace and Plasma Reactor." [Accessed 15 February 2017].

[37] Chemistry-Reference. "MOLYBDENUM(IV) SULFIDE - (1317-33-5). [Accessed 15 February 2017].

[38] Chemistry-Reference. "IRON(II) SULFIDE - (1317-37-9). [Accessed 15 February 2017].

[39] Australian Museum. “How and Why We Use the Scanning Electron Microscope (SEM).” [Accessed 8 February 2017].

[40] SEM Technology https://www.purdue.edu/ehps/rem/rs/graphics/sem2.gif [Accessed 8 February 2017].

Appendix A: TGA Data

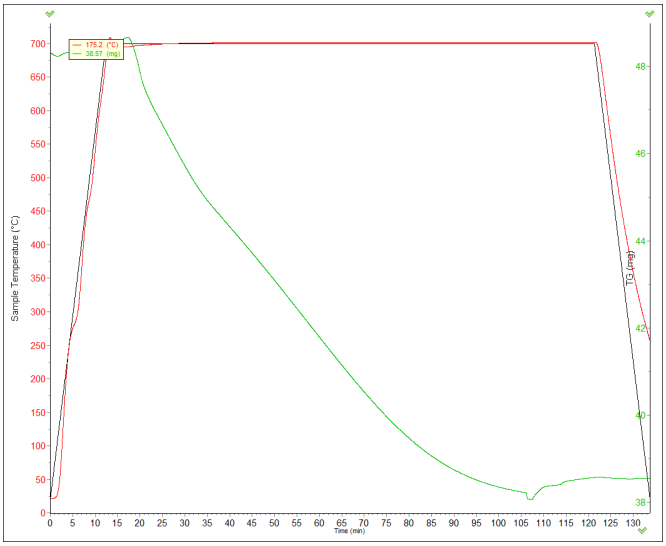

Figure A1: *TGA experiment at 700ºC for PI. Sample temperature (red line), controlled temperature (black line), and particle weight (green line) plotted over time.*

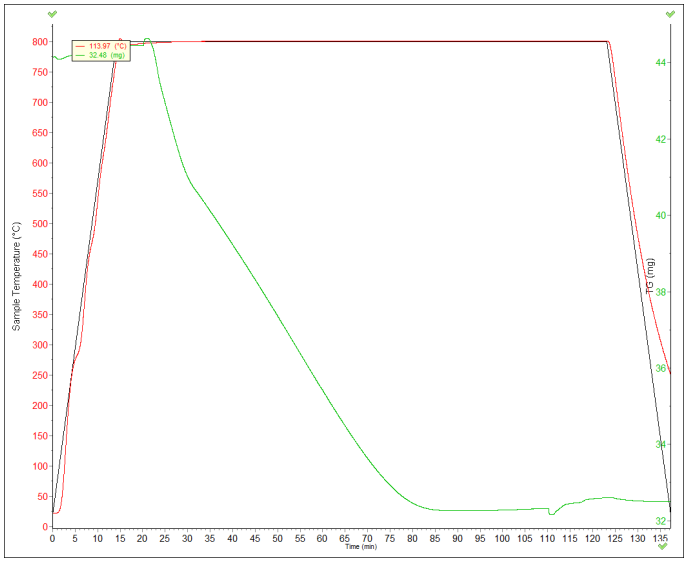

Figure A2: *TGA experiment at 800ºC for PI. Sample temperature (red line), controlled temperature (black line), and particle weight (green line) plotted over time.*

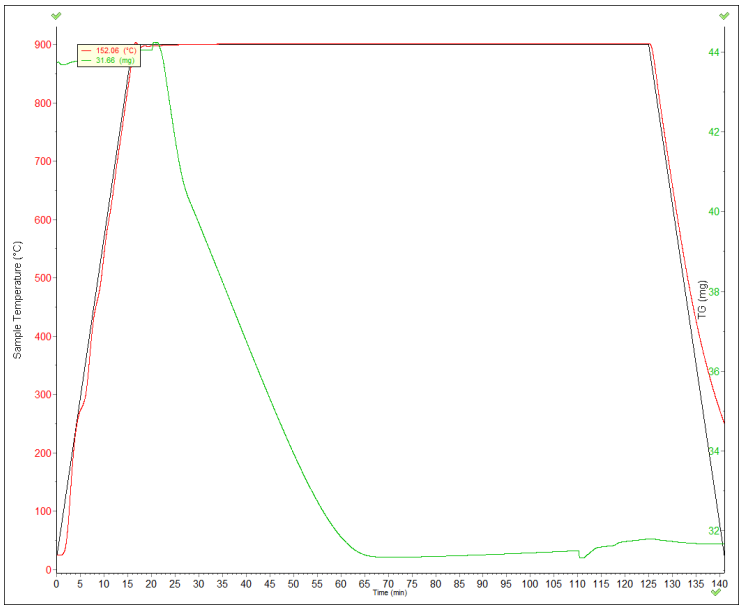

Figure A3: *TGA experiment at 900ºC for PI. Sample temperature (red line), controlled temperature (black line), and particle weight (green line) plotted over time.*

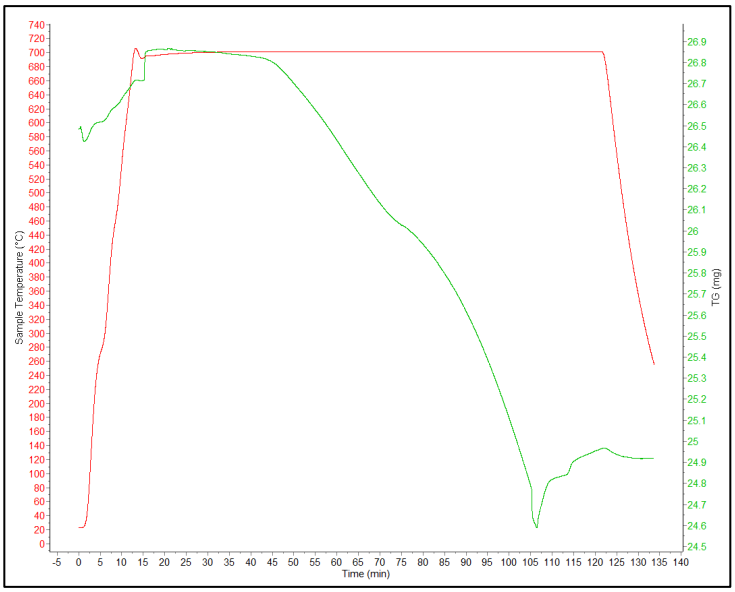

Figure A4: *TGA experiment for PIIa.i at 700ºC. Sample temperature (red line), controlled temperature (black line), and particle weight (green line) plotted over time.*

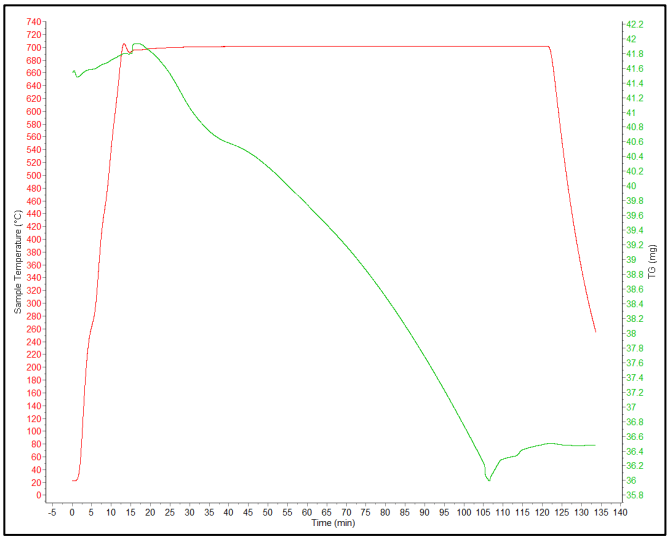

Figure A5: *TGA experiment for PIIa.ii at 700ºC. Sample temperature (red line), controlled temperature (black line), and particle weight (green line) plotted over time.*

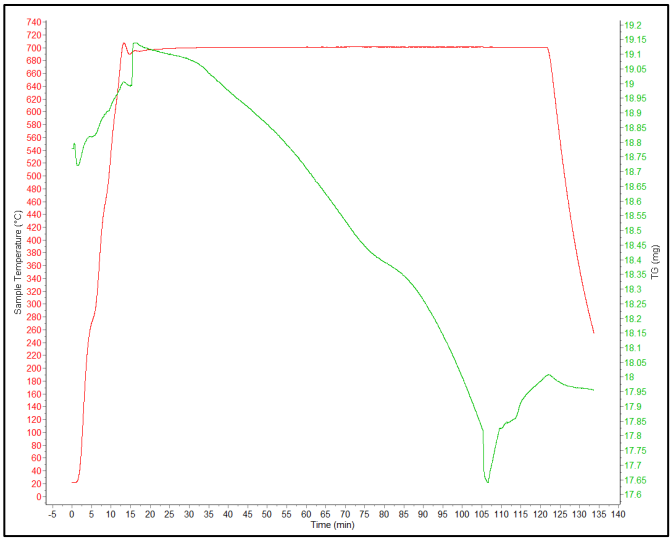

Figure A6: *TGA experiment for PIIa.iii at 700ºC. Sample temperature (red line), controlled temperature (black line), and particle weight (green line) plotted over time.*

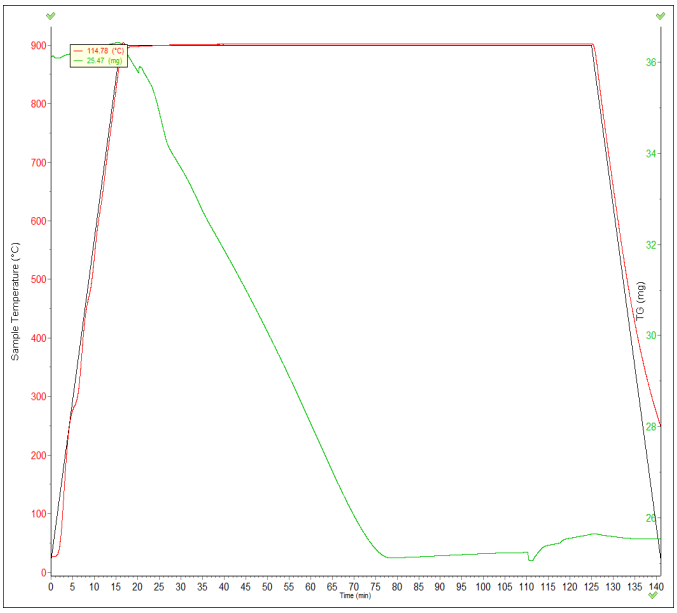

Figure A7: *TGA experiment for PIIa.i at 800ºC. Sample temperature (red line), controlled temperature (black line), and particle weight (green line) plotted over time.*

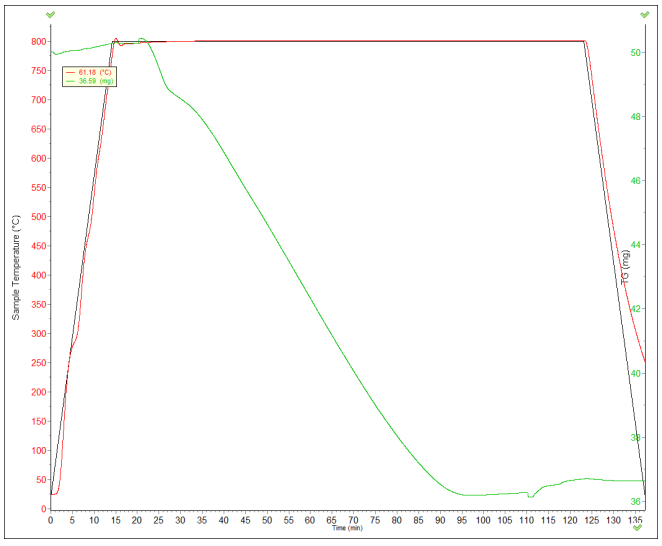

Figure A8: *TGA experiment for PIIa.ii at 800ºC. Sample temperature (red line), controlled temperature (black line), and particle weight (green line) plotted over time.*

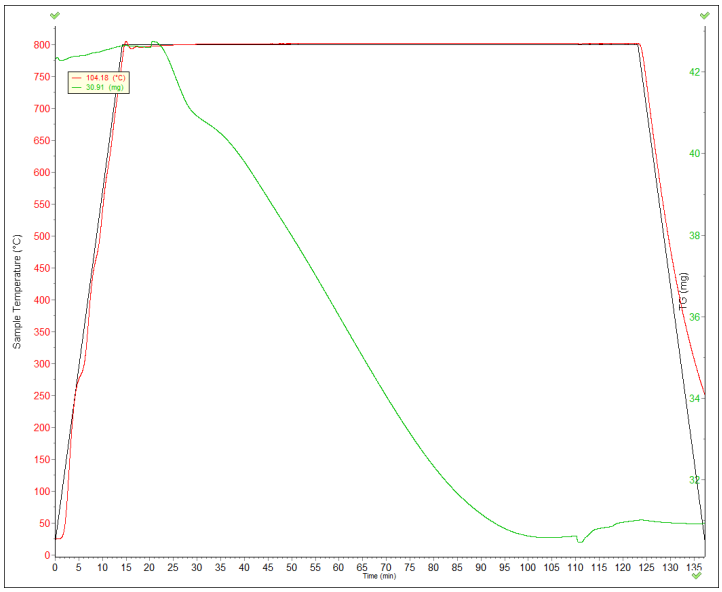

Figure A9: *TGA experiment for PIIa.iii at 800°C. Sample temperature (red line), controlled temperature (black line), and particle weight (green line) plotted over time.*

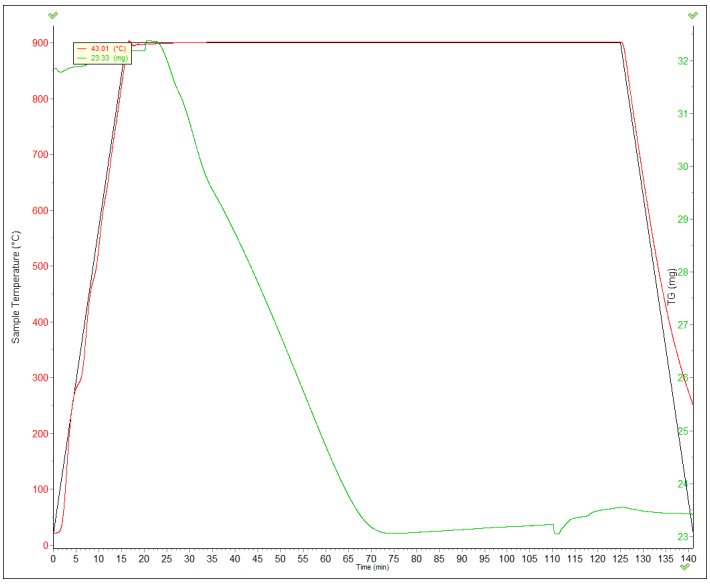

Figure A10: *TGA experiment for PIIa.i at 900°C. Sample temperature (red line), controlled temperature (black line), and particle weight (green line) plotted over time.*

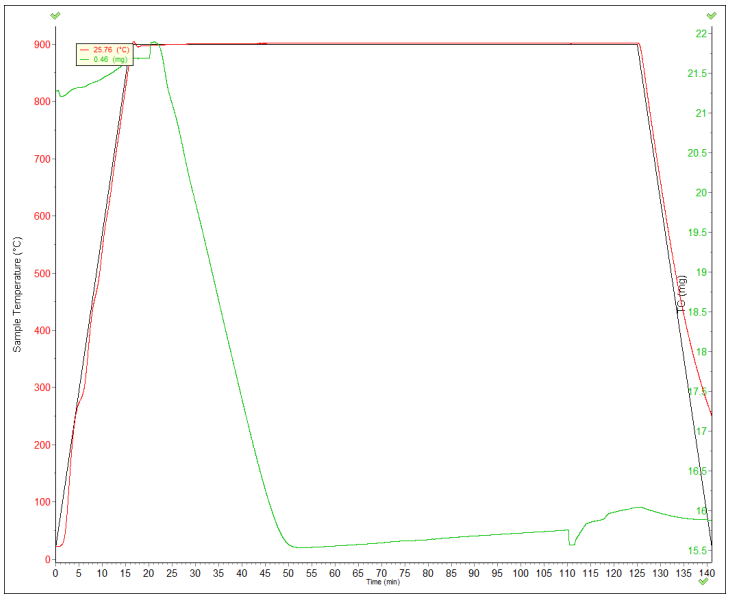

Figure A11: *TGA experiment for PIIa.ii at 900ºC. Sample temperature (red line), controlled temperature (black line), and particle weight (green line) plotted over time.*

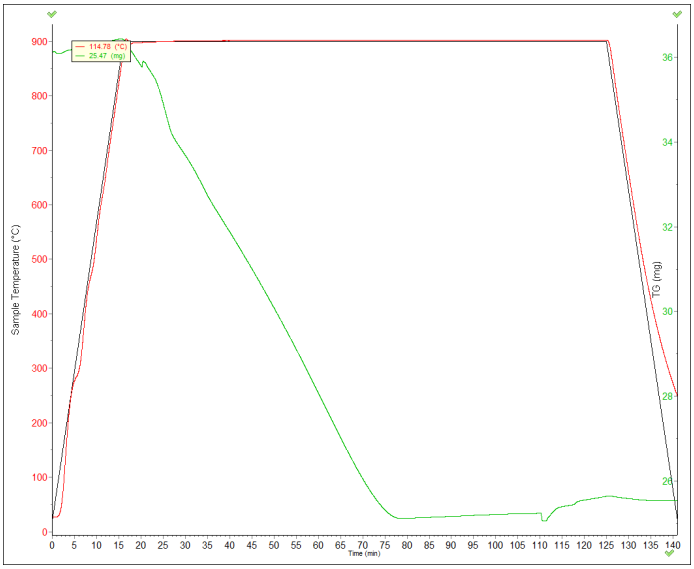

Figure A12: *TGA experiment for PIIa.iii at 900ºC. Sample temperature (red line), controlled temperature (black line), and particle weight (green line) plotted over time.*

Appendix B: XRD Data

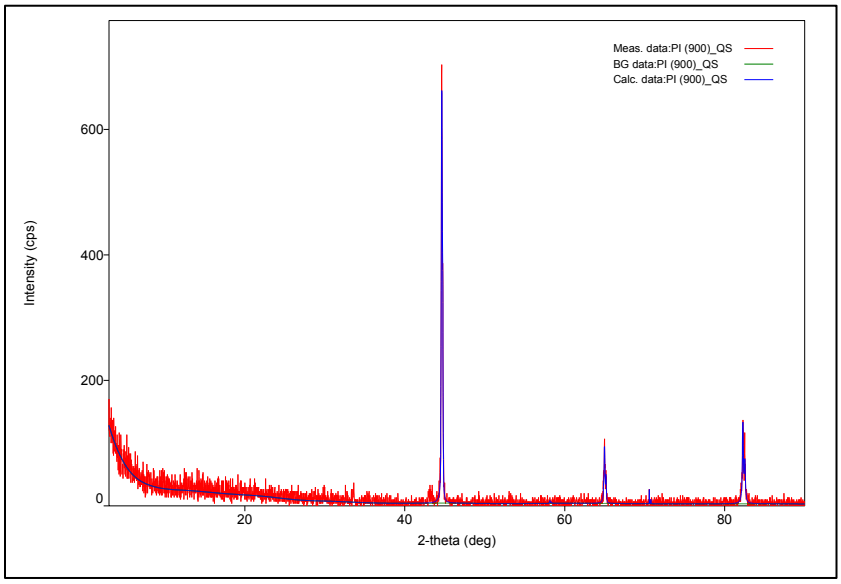

Figure B1: *Quick study of powder XRD experiment for PI at 900ºC.*

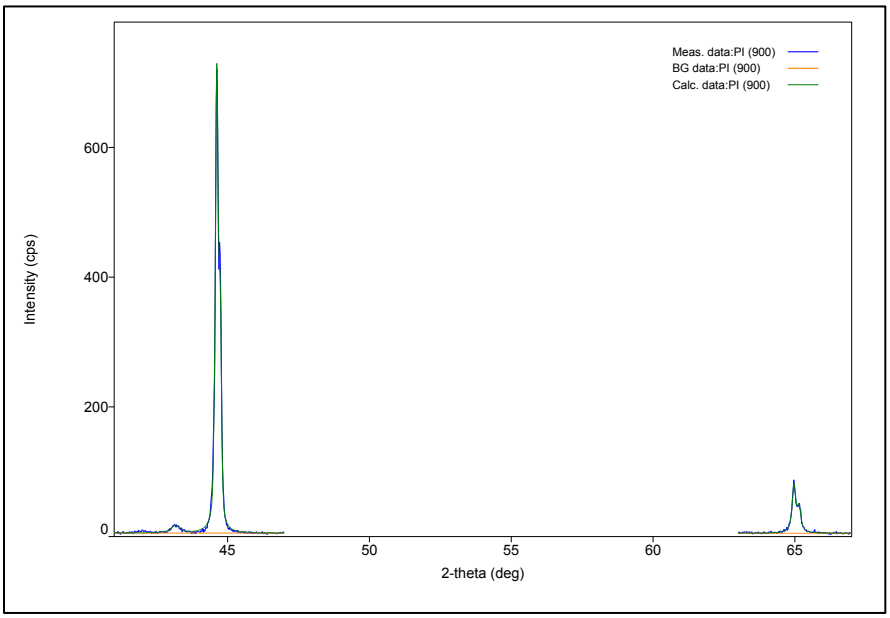

Figure B2: *Study of powder XRD experiment for PI at 900ºC.*

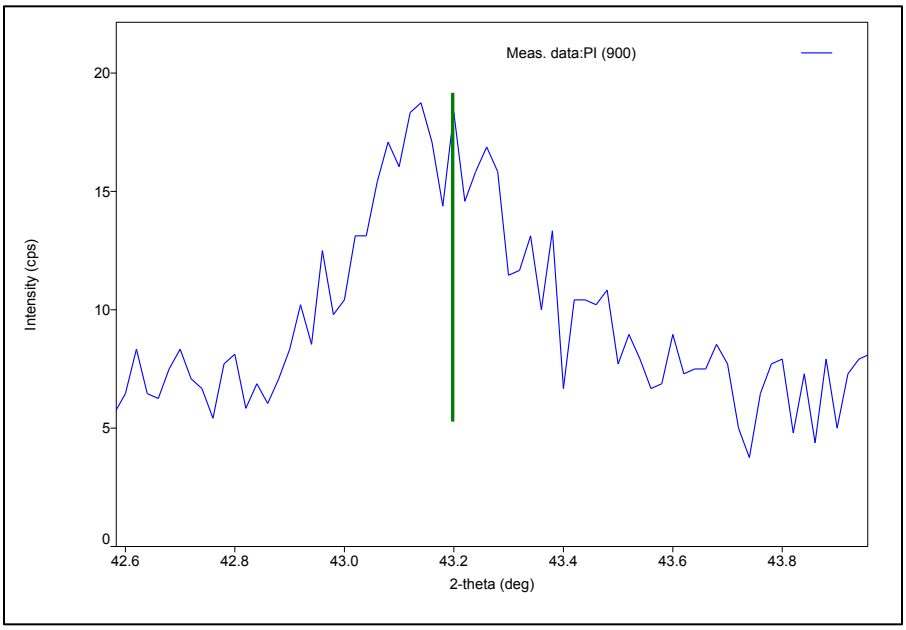

Figure B3: *Characterization of iron-sulfide (FeS) peak for PI at 900ºC.*

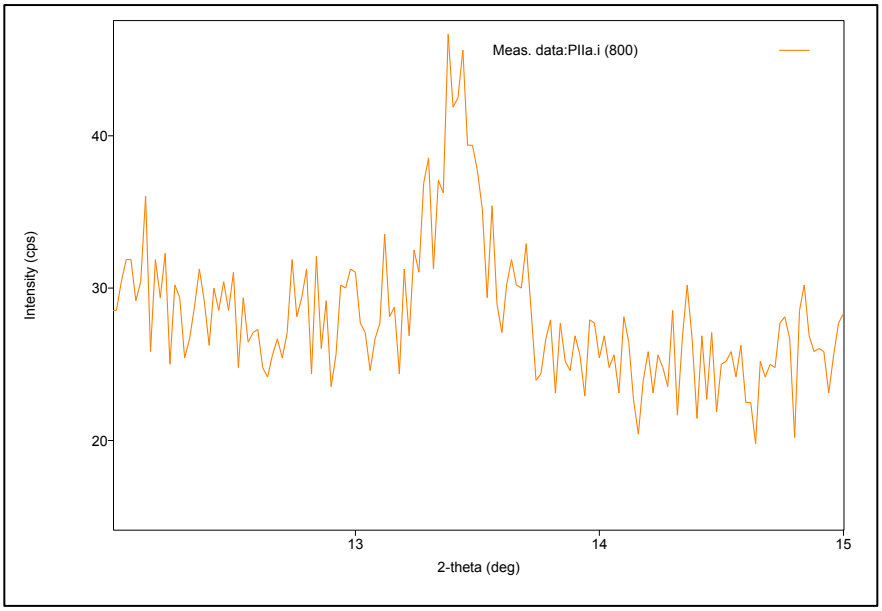

Figure B4: *Investigation of powder XRD experiment for PIIa.i at 800ºC around a 2-theta of 13.5 degrees.*

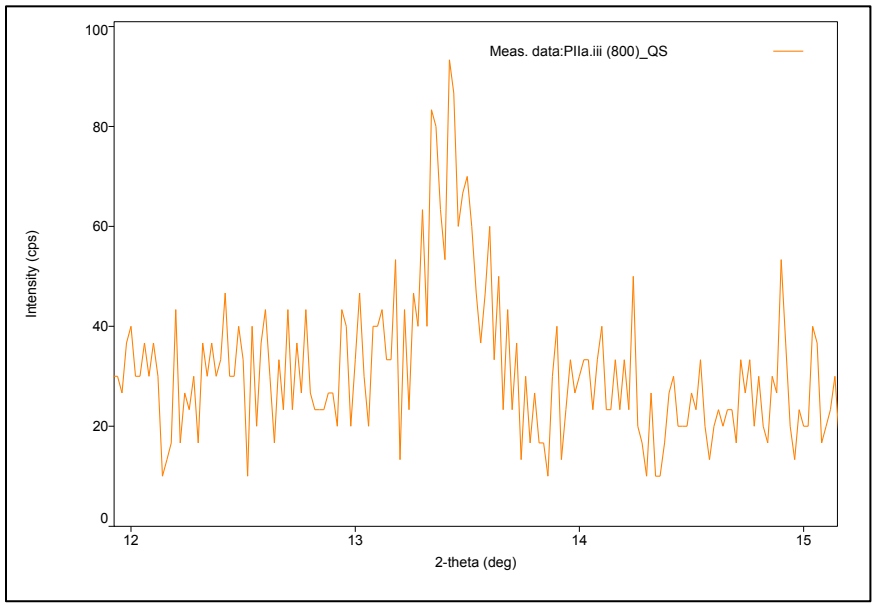

Figure B5: *Investigation of powder XRD experiment for PIIa.iii at 800ºC around a 2-theta of 13.5 degrees.*

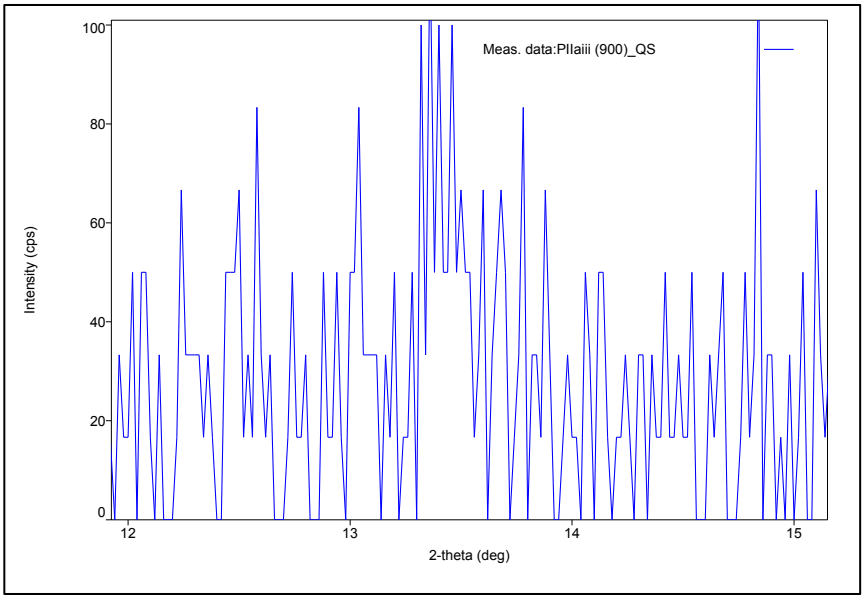

Figure B6: *Investigation of powder XRD experiment for PIIa.iii at 900ºC around a 2-theta of 13.5 degrees.*

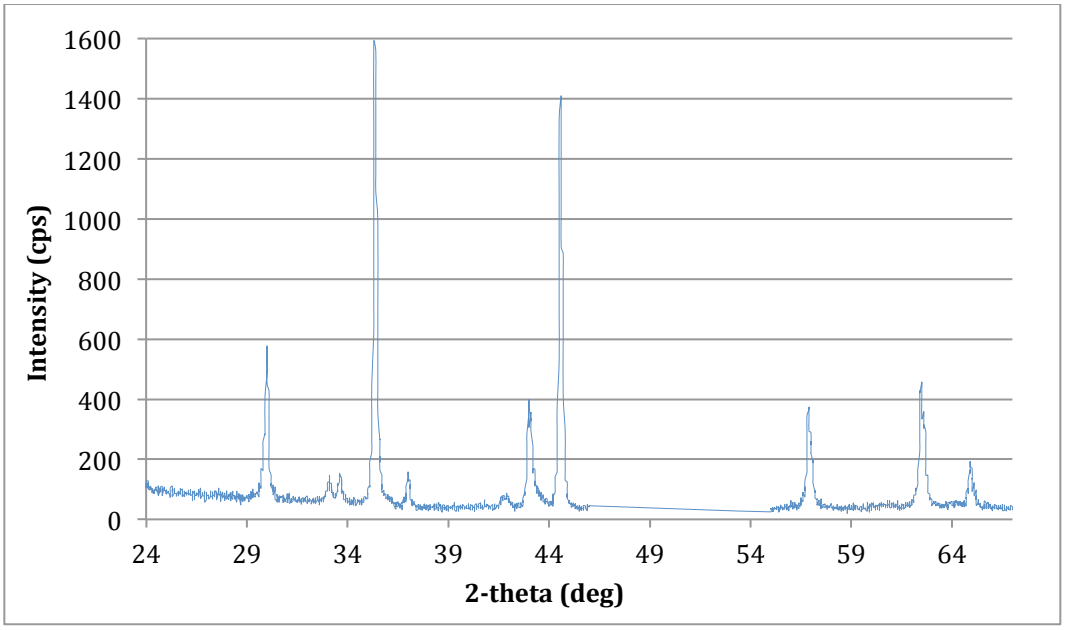

Figure B7: *Investigation of powder XRD experiment for PIIa.i at 900ºC.*

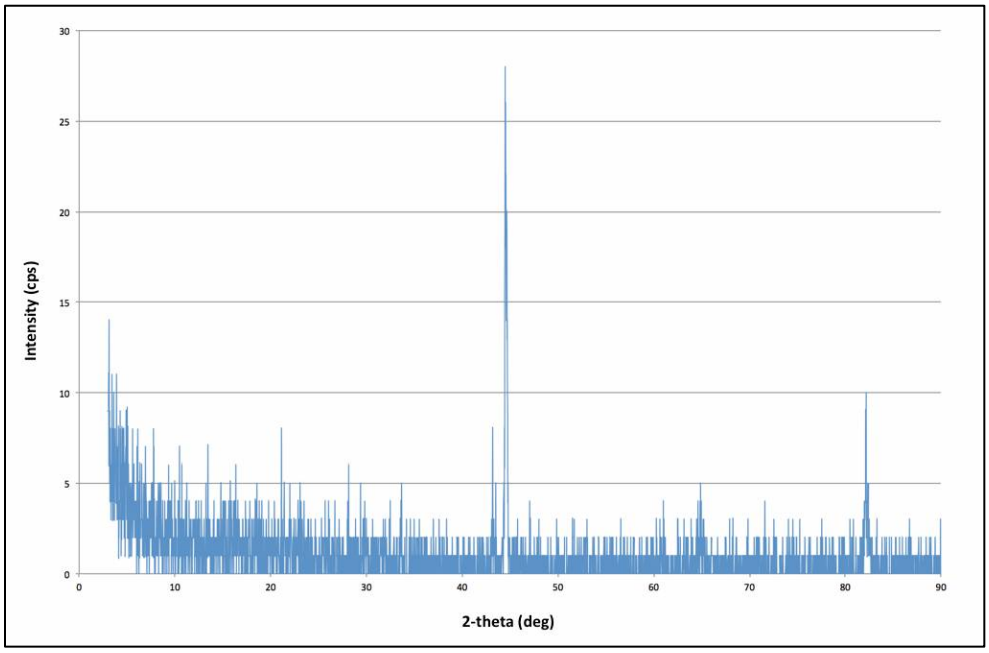

Figure B8: *Investigation of powder XRD experiment for PIIa.ii at 900ºC.*

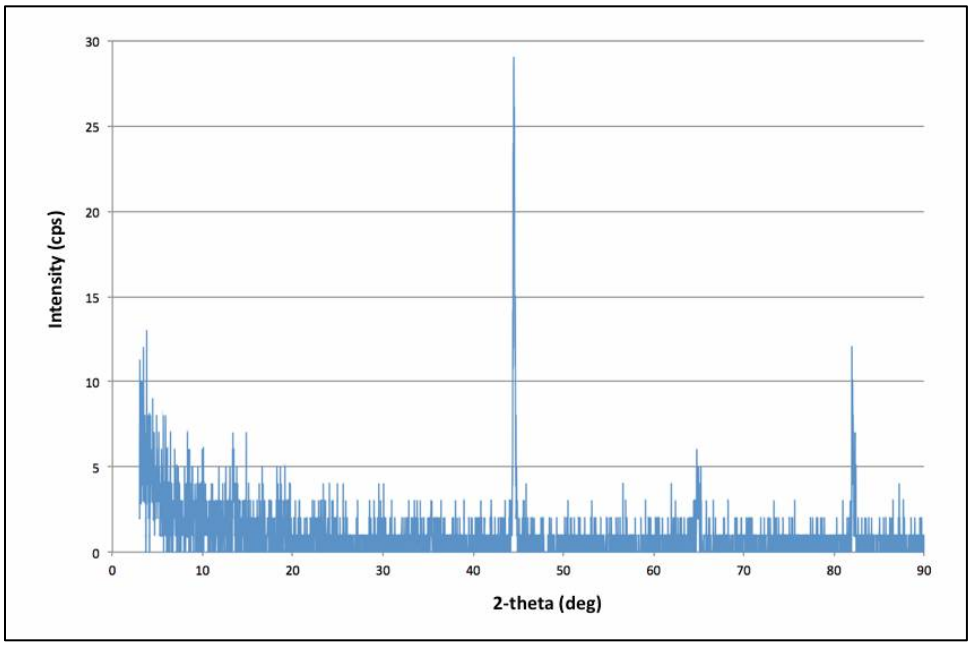

Figure B9: *Investigation of powder XRD experiment for PIIa.iii at 900°C.*